University of Copenhagen

Niels Bohr Institute

Center for Quantum Devices

Master's Thesis

Quasi Particle Tunneling in the Fractional Quantum Hall Regime

Author:
Christian J. S. Olsen

Supervisor:
Charles M. Marcus

July 1, 2015

Christian J. S. Olsen
August 23, 1988
tjv380

Abstract

The fractional quantum Hall effect occurs in clean two dimensional electron gases subjected to a perpendicular magnetic field. This rich system is 34 years after its discovery still not fully understood. Several problems still remain open after many years of serious attention from both experimentalists and theorists. It is therefore wroth investigating the seemingly basic questions, from which we still have a lot to learn. In this thesis investigations of excitations in the fractional quantum Hall effect is presented.

In Chapter 1 I give an introduction to the two dimensional electron gas, the classical Hall effect and the quantum Hall effect. Chapter 2 is devoted to the quantum point contact (QPC). Firstly I give an introduction to the basics of the QPC, followed by data showing many robust conductance steps at zero bias and a link between the 0.7 structure in the first subband and finite bias features in the second.

Quasi particle tunneling can provide us with crucial information about the origin of the host state and help us distinguish between different proposed wavefunctions for the lesser understood states. In the first part of Chapter 3 I present quasi particle tunneling measurements of $\nu = 1/3$ in a QPC. The last part of Chapter 3 is reserved for measurements of several fractional states in the strong backscattering regime.

Contents

List of Figures

List of Tables

Acknowlegdments

I started my life in experimental physics at Center for Quantum Devices (QDev) when it was still in its infancy. In that sense it is save to say that I owe all my current experimental knowhow to the people of QDev. One man stands out, Charlie Marcus. He offered me the chance to be a part of his new adventure in Denmark and I gladly took it. For that opportunity I am grateful! Charlie has personally taught me the ways of the quantum Hall effect and has over the years given me great advise whenever I needed it.

I still remember the early days where all daily tasks were connected to putting thing into drawers and setting up the lab in general. The one thing that stands out clearest is how Ferdinand with an admirable patience guided everybody around and like a magician pulled a fully functioning lab from his hat. I owe Ferdinand a great thanks for all his help especially in the beginning where everything was new.

Katrine have been my FQHE partner from the beginning. I want to thank her for a good and fun collaboration over the years. Also Charlotte, Konstanteen and Paul do I owe a thanks for great discussions and collaboration.

Morten K also deserves my gratitude, not only did he introduce me to Charlie, he has also always been helpful especially as my in house theory goto guy.

The Wednesday crew: Henri, Giulio, Thorvald, Christian Volk and Johannes have always been ready when Oak Room summoned us for a drink (mostly two). I have enjoy these evenings and I owe you all thanks for spending them with me.

Shivendra have first as a Ph.D student and later as the cleanroom and fabrication

CEO helped me a lot with fab and have in general been willing to help out if he could. I still owe him a cake from the small mask incident (I don't want to talk about it!). Andrew and Willy also deserves my gratitude, they have always been helpful in the lab and I have benefited greatly from their help.

Lastly, I want to thank Josh and Silvia for a great year. They were in their time in QDev a big help for the FQH team.

Chapter 1

Introduction

Many of the most fascinating quantum mechanical phenomenons are seen in many body systems, such as the ones found in nano sized semiconducting devices. In these systems the phenomenons can be probed by simple electrical measurements, without the need of multi billion dollar particle accelerators. Most of these phenomenons originate from the electron-electron interaction, governing the subtle and sometimes fragile physics that gives rise to these amazing effects. An example is Superconductivity, where the electron-phonon interaction mediates an attractive electron-electron interaction. This makes it favorable for the electrons to form Cooper pairs and Bose condense[1]. The striking experimental signature is electrical conductance without dissipation (zero resistance). Another intriguing effect is found in Mott insulators. Here electron-electron interactions lead to band gap insulators in partially filled band materials[2].

The most interesting effect of them all, is the quantum Hall effect (QHE). The richness of this system exceeds all other, which manifests itself in the fact that even today, 34[1] years after its discovery, scientists are still far from understanding the full extent of the physics influencing the system. Apart from the interger quantum Hall effect (IQHE), which is a single particle effect, all other features associated with the QHE are governed by the electron-electron interaction. The fractional quan-

[1]The fractional quantum Hall effect was discovered in 1981, by D. C. Tsui and coworkers[3].

tum Hall effect (FQHE) originates from electron-magnetic flux interaction, which reduces the effective Coulomb repulsion between the electrons[4]. The re-entrant interger quantum Hall effect (RIQHE), seen at filling factor $\nu > 2$. The effect is believed to arise from bubble phases, where electrons, in the partial filled spin split Landau level (LL), form super Wigner crystals in order to reduce the Coulomb repulsion between individual crystals[5]. And lastly the stripe phases, responsible for anisotropic transport, seen at half filling in the second and third LL[5].

In this thesis I present the results of several experiments I have performed during my Masters. The experiments range from studies of quantum point contacts (QPCs) to quasi particle tunneling in the fractional quantum Hall regime. In the rest of the Introduction (Charter 1), I will explain the basics of the two dimensional electron gas (2DEG). The theory needed to understand the Hall effect, classical and quantum, will also be presented. Chapter 2 will detail the studies I have done in QPC geometries, showing zero bias anomalies at low conductance and 0.7 structure physics at elevated temperatures. Chapter 3 will be devoted for quasi particle tunneling in QPCs, both in the weak and strong backscattering regimes. The main focus of the weak backscattering experiments is on filling factor $\nu = 1/3$, whereas a broader range of states are studied in the strong backscattering regime.
Appendix A will detail my fabrication recipes, as well as my thoughts and considerations concerning semiconductor fabrication.

1.1 The two dimensional electron gas

The two dimensional electron gas is the perfect host system for measuring quantum mechanical effects, such as quantum dots, QPCs and of cause the quantum Hall effect. As the name suggest the 2DEG, is a strictly two dimensional system of free electrons. The "free" part should be taken literally, as the electrons in these systems can have a mean free path on the order of millimeters. One of the best features of

the 2DEG is the possibility of gating. Metal gates can be used to define areas where the density can be locally changed, which can be used to define small islands with reduced dimensionality as needed for structure like quantum dots and QPCs.

The most common ways of achieving a 2DEG are by using a metal-oxide-semiconductor field-effect transistor (MOSFET) or a semiconducting heterostructure. The MOSFETs are not used anymore due to poor 2DEG qualities. The best 2DEGs are found in gallium arsenide/aluminium gallium arsenide (GaAs/AlGaAs) heterostructures. The different band gaps of GaAs and AlGaAs can be used to form a potential well, in which the electron gas resides. The small difference in lattice constants between GaAs and AlGaAs insures that there is a minimum of strain between the layers in the crystal. Strain induces crystal imperfections, which will reduce the electrons mobility by scattering.

All GaAs/AlGaAs heterostructures are grown with atomic layer precision using molecular beam epitaxy (MBE), typically a wafer is grown on an existing GaAs substrate. Directly on top of the substrate a superlattice, of many thin alternating GaAs and AlGaAs layers, are grown. The purpose of the superlattice is to trap any impurities from the substrate, which would otherwise act as scattering sites for the electrons in the 2DEG[6]. Am AlGaAs spacer layer is put on top of the superlattice. Here electron doners, typically Silicon atoms, are added in a single atomic layer (δ-doping). There are two doping methods, either the Si atoms are put directly into the space layer or they are introduced in small doping wells. The wells consist of aluminum arsenide (AlAs) covered a thin layer of GaAs on both sides.

There are pros and cons involved in using either of the two doping schemes. Putting the doping atoms directly into the spacer layer will create DX centers. DX centers are a lattice defect induced by the donor atom. The extra electron, from the Si atom, is tightly bound to the defect site, which makes it less likely to diffuse to the 2DEG[7]. Therefore this method is often used for low density 2DEGs. The drawback is a reduced mobility, because the donor atoms act as scattering sites for

the 2DEG electrons[8]. The doping wells offer a solution to the reduced mobility problem. Not all the extra electrons will diffuse to the 2DEG, a lot will stay in the doping wells, screening the donor atoms[7]. However, the left over donors in the doping wells are less tightly bound, which can result in gate stability issues.

The main quantum well, holding the 2DEG, is grown next. This can either be a symmetric well, using an AlGaAs/GaAs/AlGaAs sandwich or a asymmetric well formed on the boundary between an AlGaAs and an GaAs layer. The GaAs layer used for the symmetric well is usually 30 nm to 50 nm wide. More donors can be introduced in a similar fashion as below the 2DEG and the full structure is caped with a layer of GaAs. A schematic of a typical wafer composition, with symmetric doping directly inserted in the AlGaAs spacer layer, along with a energy diagram is shown in fig. (1.1).

In order to ensure a 2 dimensional system, the Fermi level must lie between the ground state and first excited state of the quantum well. The bandgap difference between AlGaAs and GaAs is 300 meV to 400 meV[9], depending on the Al concentration. If we assume that this energy is much bigger than anything else and ignore the curved bottom, we can approximate the quantum well with an infinite square well. The allowed energies are:

$$E_n = \frac{n^2\pi^2\hbar^2}{2m^*d^2},$$

where d is the width of the well and $m^* = 0.067m_e$ is the effective electron mass in GaAs[9]. The energy of the two first energy levels for $d = 50\,\text{nm}$, is $E_1 = 2.25\,\text{meV}$ and $E_2 = 8.99\,\text{meV}$. The Fermi energy in two dimensions is $E_F = \frac{\hbar^2\pi n}{m^*}$, where n is the electron density. Using a typical density of $n = 1 \times 10^{11}\,\text{cm}^{-2}$ yields a Fermi energy of $E_F = 3.54\,\text{meV}$, well within the limit. When typical operating temperatures (not higher than $100\,\text{mK} = 8.6\,\mu\text{eV}$) are taken into account, is it clear that the second energy level of the well never will be populated.

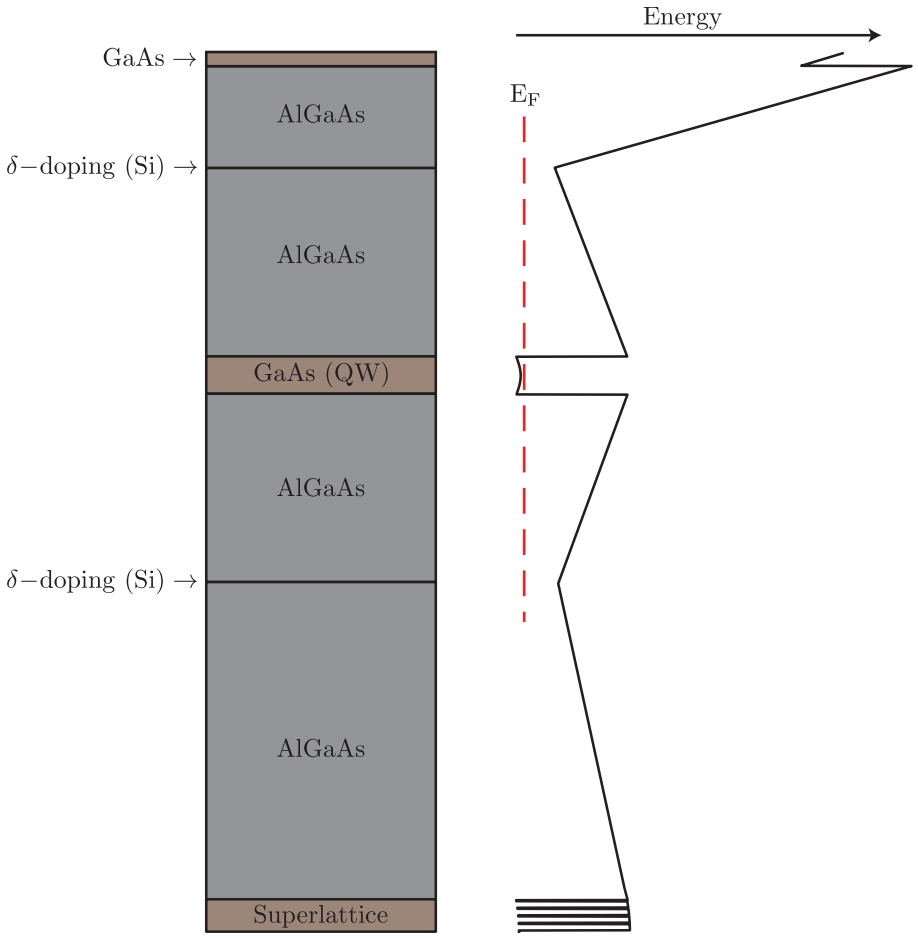

Figure 1.1: GaAs/AlGaAs quantum well structure, with corresponding energy diagram. The red dashed line shows the Fermi level. The energy diagram was calculated using a Schördinger/Possion solver.

1.2 The quantum Hall effect

Long before the discovery of the quantum Hall effect, E. Hall discovered the classical Hall effect in 1879[10]. He did so by running a current through a gold leaf, while measuring the voltage drop across the current direction. He measured a finite constant voltage when turning on a perpendicular magnetic field. A similar setup is shown in fig.(1.2a), where the voltage drop E. Hall measured is labeled V_{xy}.

E. Halls discovery can be understood in the context of the Drude model[11], here simplified to two dimensions. The equation of motion for an electron in an

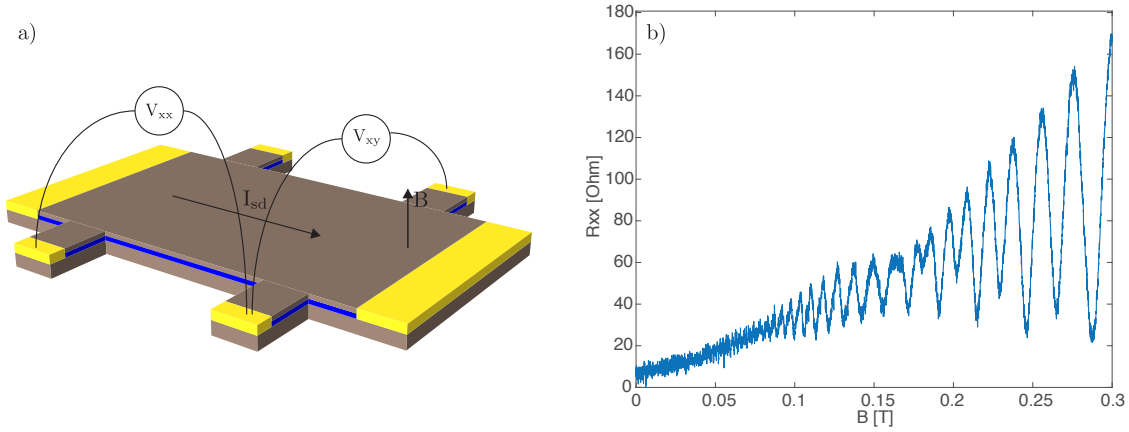

Figure 1.2: a) Schematic representation of a measurement of the classical Hall effect. The voltage V_{xy} will only be non-zero when a perpendicular magnetic field is present. The current run in the 2DEG, blue layer below the surface. b) Measurement of the longitudinal resistance, obtained from the voltage along the current. 70 mT marks the transition from classical to qauntum.

external electric and magnetic field is described by the Lorentz force:

$$m^* \frac{d\mathbf{v}}{dt} = -|e| \left(\mathbf{E} + \mathbf{v} \times \mathbf{B}\right). \tag{1.1}$$

The solution of eq. (1.1) is valid in between scattering events. Pointing the magnetic field in the z direction, $\mathbf{B} = (0, 0, B)$, and the electric field along the x direction, $\mathbf{E} = (E, 0, 0)$ and introducing a mean scattering time τ, we can calculate the drift velocities[12]:

$$\begin{aligned} \hat{v}_x &= -E \frac{\mu}{1 + \omega_c^2 \tau^2} \\ \hat{v}_y &= v_D \frac{\omega_c^2 \tau^2}{1 + \omega_c^2 \tau^2}, \end{aligned} \tag{1.2}$$

where $\omega_c = |e|B/m^*$ is the cyclotron frequency, $v_D = E/B$, and $\mu = |e|\tau/m^*$ is the mobility. Using the relationship between applied electric field and the current

density:

$$\begin{pmatrix} E_x \\ E_y \end{pmatrix} = \begin{pmatrix} \rho_{xx} & \rho_{xy} \\ -\rho_{xy} & \rho_{xx} \end{pmatrix} \begin{pmatrix} j_x \\ j_y \end{pmatrix}, \tag{1.3}$$

where $j_\alpha = -|e|n\hat{v}_\alpha$, ρ_{xx} is the resistivity along the x direction and ρ_{xy} is the resistivity along the y direction. Using eq. (1.2) and eq. (1.3) we can find an expression for the resistivities:

$$\begin{aligned} \rho_{xx} &= \frac{m^*}{ne^2\tau} \\ \rho_{xy} &= \frac{B}{|e|n}. \end{aligned} \tag{1.4}$$

The first 70 mT of fig. (1.2b) shows a measurement of a 2DEG in the classical regime. The classical Hall measurement is widely used to determine the carrier density and mobility, as well as the sign of the carriers.

In our high purity samples, the classical theory is only valid for $< 70\,\mathrm{mT}$. For $B > 70\,\mathrm{mT}$ quantum effects takes over, which strongly modifies the response of the system. The first sign of the transition from classical to quantum are the Shubnikov-de Haas (SdH) oscillations. The SdH oscillations are seen in the longitudinal resistivity when the Landau level splitting becomes larger than the broadening due to scattering and disorder. When this happens the density of states (DOS) will show modulations, which will result in an oscillating longitudinal resistivity. At higher magnetic fields, where the energy quantization becomes dominant, marks the onset of the integer quantum Hall effect.

1.2.1 The integer quantum Hall effect

Before getting into quantization of Hall effect and what that implies to the measured resistances, is it worth solving the Schrödinger equation for electrons in a

perpendicular magnetic field. The Hamiltonian describing the system is:

$$H = \frac{1}{2m^*}\left(\mathbf{p} + |e|\mathbf{A}\right)^2 + V(z), \tag{1.5}$$

where $\mathbf{p} = -i\hbar\nabla$ is the canonical momentum, $\mathbf{A}$ is the vector potential and $V(z)$ is the confinement potential in the z direction. The Schrödinger equation is gauge invariant, which means we have the freedom to choose a vector potential as long as it fulfills $\nabla \times \mathbf{A} = \mathbf{B}$. Lets choose the perpendicular direction to be the z direction. Furthermore lets choose to work in the Landau gauge, $\mathbf{A} = -By\hat{x}$, this leads to a separable Hamiltonian,

$$\begin{aligned} H &= H_z + H_{xy} \\ H_z &= \frac{p_z}{2m^*} + V_z \\ H_{xy} &= \frac{1}{2m^*}\left(\left(p_x - |e|By\right)^2 + p_y^2\right). \end{aligned} \tag{1.6}$$

Solving H_z gives the solution to in the confinement potential with energies $E_z = \frac{\hbar k_z}{2m^*}$. As noted in sec. (1.1) only the ground state in the z direction will be occupied and we can ignore this contribution going forward.

The Hamiltonian in the plan, eq. (1.5), commutes with p_x and we can therefore replace $p_x = \hbar k_x$ by its eigenvalue. Rewriting eq. (1.5) in terms of the cyclotron frequency, $\omega_c = \frac{|e|B}{m^*}$, and the magnetic length, $l^2 = \frac{\hbar}{|e|B}$, we arrive at:

$$H_{xy} = \frac{\hbar\omega_c}{2}\left((lk_x)^2 + \left(\frac{y}{l}\right)^2 - 2k_x y + \frac{lp_y^2}{\hbar}\right). \tag{1.7}$$

Identifying new variables, $\bar{y} = \frac{y}{l} - lk_x$ and $\bar{p}_y = \frac{lp_y}{\hbar}$, eq. (1.7) simplifies to[4]:

$$H_{xy} = \frac{\hbar\omega_c}{2}\left(\bar{y}^2 + \bar{p}_y^2\right), \tag{1.8}$$

the one dimensional harmonic oscillator, with center coordinate $y_0 = l^2 k_x$. The allowed energies for a harmonic oscillator are:

$$E_n = \hbar\omega_c \left(n + \frac{1}{2}\right), \tag{1.9}$$

with eigenstate described by plane waves in the x direction and a localized harmonic oscillator in the y direction,

$$\begin{aligned} \psi_{n,k_x}(x,\bar{y}) &= e^{ik_x x}\chi_{n,k_x}(\bar{y}) \\ \chi_{n,k_x}(\bar{y}) &= \frac{1}{\sqrt{2^n n!}}\left(\frac{1}{\pi l^2}\right)^{1/4} e^{-\frac{\bar{y}^2}{2l^2}} H_n(\bar{y}). \end{aligned} \tag{1.10}$$

H_n are the Hermite polynomial of order n. The energy levels in eq. (1.9) are called Landau levels (LL) and if we include the Zeeman splitting the eigenenergies then are:

$$E_n = \hbar\omega_c \left(n + \frac{1}{2}\right) \pm \frac{1}{2} g^* \mu_B B, \tag{1.11}$$

where $\mu_B = \frac{\hbar|e|}{2m_e}$ and g^* is the effective g factor. Fig. (1.3) shows the evolution of the DOS as a magnetic field is turned on and disorder is introduced. Disorder will broaden the δ-function shaped DOS peaks and close the energy gaps, fig. (1.3d). The states lying the tails of the broadened DOS are localized and will not take part in the transport, gray regions in fig. (1.3d). Only states close to the maxima are extended and hence can contribute to transport[4]. We say that the localized states form a mobility gap.

The LL energies, eq. (1.9), do not depend on k_x and each LL will therefore be highly degenerate. In order to calculate the degeneracy of each LL, we must assume periodic boundary conditions in the x direction[4], $e^{ik_x(x+L_x)} = e^{ik_x x}$. This gives us the allowed value of $k_x = \frac{2\pi}{L_x N}$, where N is an integer. By remembering that the states are localized at $y = k_x l^2$, we can count the number of available states in an

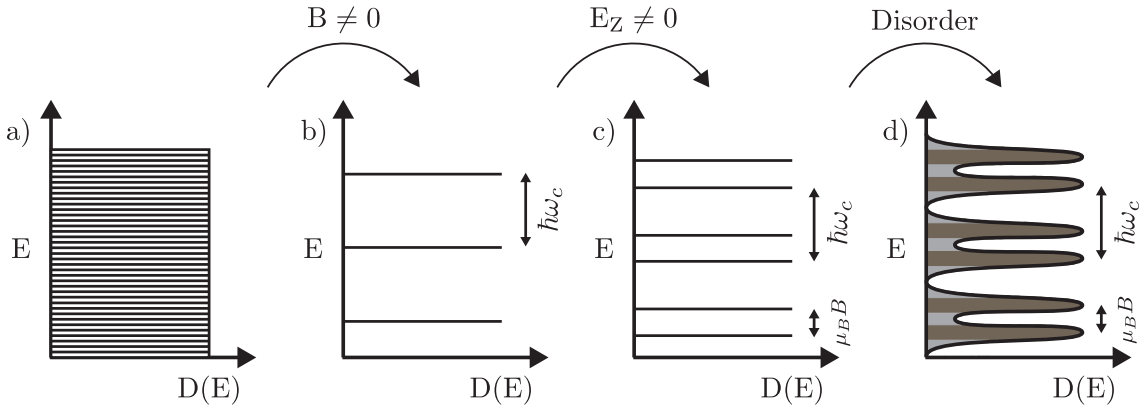

Figure 1.3: a) DOS of a 2DEG. b) δ-function shaped DOS in a perpendicular magnetic field (LL). c) Splitting of the DOS by the Zeeman term. d) The spin split LL broadened by disorder, gray areas are localized whereas brown areas are extended states.

area $A = L_x L_y$. The state at $y = 0$ is labeled by $N = 0$ and the state at $y = L_y$ by $k_x = L_y/l^2$. This leads to:

$$N = \frac{L_x L_y}{2\pi l^2}, \tag{1.12}$$

the number of states in an area A. The degeneracy per unit area is then:

$$n_L = \frac{1}{2\pi l^2} = \frac{B}{\phi_0}, \tag{1.13}$$

where $\phi_0 = h/e$ is the flux quantum. Because the degeneracy is proportional to the magnitude of the magnetic field, the available space in each LL will increase as the magnetic field is increased, hence the LL's will depopulate.

The filling factor is defined as, $\nu = n/n_L$, the number of electrons per flux quantum penetrating the sample. The filling factor is used to keep track of the number of occupied spin split LL. At $\nu = 1$ the lowest spin split LL is fully occupied, whereas at $\nu = 2$ the first LL is fully occupied.

As discovered by K. von Klitzing et. al. in 1980[13], the resistance measured

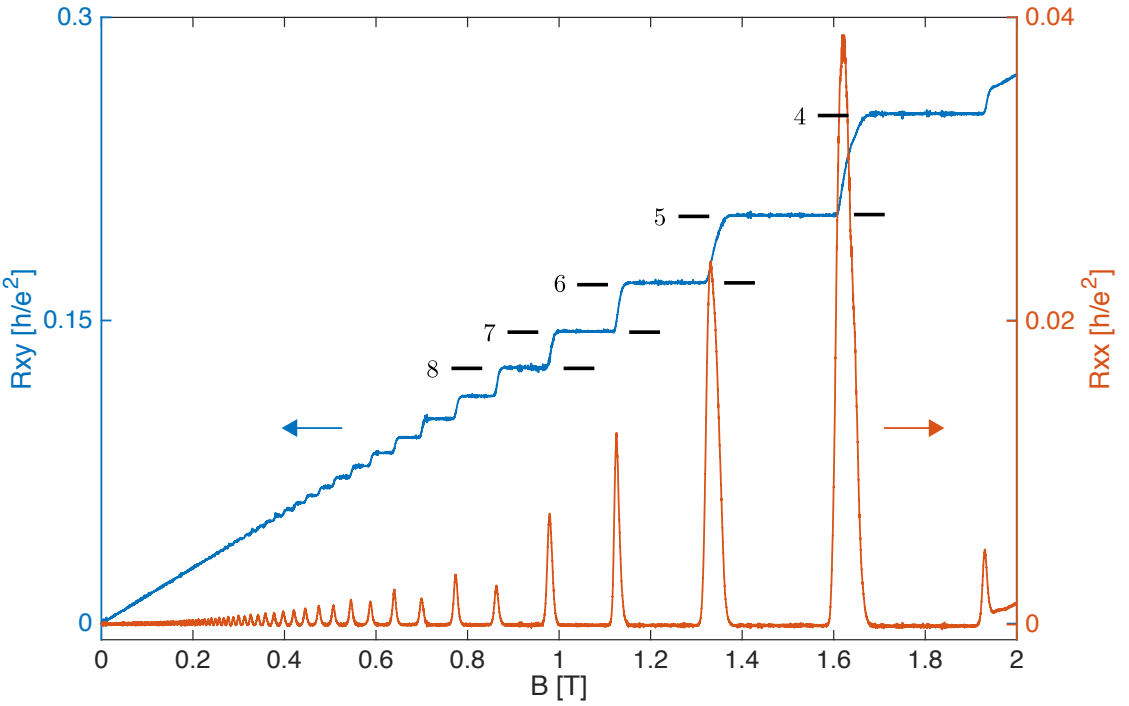

Figure 1.4: Measurement of the IQHE. Rxx (orange) is zero whenever Rxy (blue) is at a plateau. The plateaus corresponding to $\nu = 4 - 8$, are marked.

across the current direction, R_{xy}, is quantized in multiples of h/e^2:

$$R_{xy} = \frac{1}{\nu}\frac{h}{e^2}. \tag{1.14}$$

They also found that the resistance along the current direction, R_{xx}, was zero whenever R_{xy} was quantized. The non-zero width of these quantized plateaus (and the corresponding regions with zero resistance) is due to the mobility gap. When increasing the magnetic field away from the exact filling, the states that are depopulated are localized states, which do not contribute to transport. Only after all the localized states are depopulated will the quantization be broken by the depopulation of extended states. The quantization of the integer plateaus have been measured to a relative accuracy of 10^{-8}. This is also why the quantum Hall effect is used to define the Ohm. Fig. (1.4) shows a measurement of the integer quantum Hall effect.

In many systems this fact is not very important, but in order to understand the quantum Hall effect the edges are essential. This was realized shortly after K.

von Klitzings discovery [14]. At the sample edge the LL's must bend up because the potential energy of the confinement diverges. The bending of the LL's are schematically shown in fig. (1.5a-c). The LL's intersect with the Fermi energy close to the edge and form one dimensional conduction channels. These channels are dissipationless due to the chirality of the edge states and the exponential suppression of the backscattering across the bulk. In the bulk of the sample the occupied LL's are now energetically far away from the Fermi energy, which leaves the internal part of the sample insulating. The electrons in the edge states propagate with a group velocity determined by the confinement potential V_{con} and is given by[12]:

$$v_x = \frac{1}{\hbar}\frac{\partial V_{con}}{\partial k_x}, \tag{1.15}$$

and each edge state contribute h/e^2 to the measured resistance.

In 1992 D. B. Chklovskii et al.[15] improved the edge state theory, by taking electron-electron interaction into account. They showed that the simple picture of bending LL's near the edge was too crude and lacked the ability to explain relaxation between copropagating edge states. Their results are presented in fig. (1.5d-f). Instead of one dimensional edge channels, they found strips of finite width, where the LL's get pinned to the Fermi energy. These regions are compressible due to the existence of unoccupied extended states. In the compressible strips the varying potential is well screened by the extended states and therefore the density increases smoothly, going away from the sample edge. In the regions where the LL's have a slope they found incompressible strips, where no extended states are available. The lack of screening in these regions lead to a varying confinement potential, but a constant density. In the model by Chklovskii et al. the density profile in the QH regime is only slightly modified compared to the zero field density profile. Whereas the naive bending picture produces very abrupt changes in the density profile, see fig. (1.5c,f).

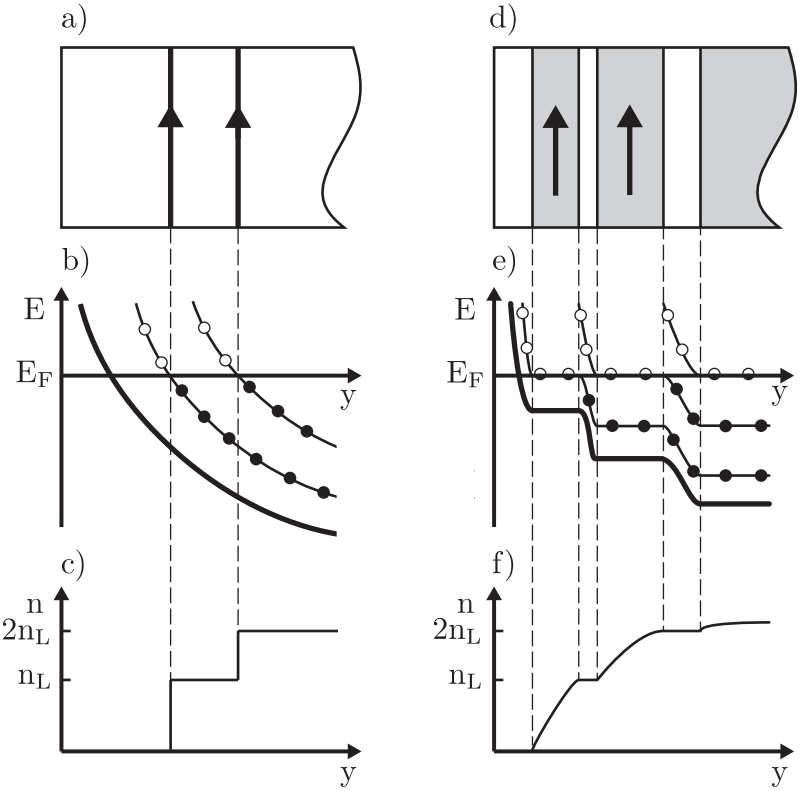

Figure 1.5: a)-c) Naive edge state picture. a) Top view onto a 2DEG near an edge. b) Bending of the LL's due to the confinement potential. Circles represent local filling. c) Density profile close to the edge. d)-f) The Chklovskii/Shklovskii/Glazman edge state picture. d) Top view onto a 2DEG near the edge. Alternating incompressible (gray) and compressible (white) strips. Arrows shows the direction of the electron flow. e) Bending of the potential and LL's near the edge. Circles represent local filling. f) Density profile close to the edge. Compressible strips have a non-uniform density profile and carry the flow of electrons. The incompressible strips have constant density that matches the filling factor. Adapted from [15].

1.2.2 The fractional quantum Hall effect

What happens after $\nu = 1$ you may ask. In terms of LL's nothing should happen. All electrons are already contained in the lowest spin split LL, so increasing the field should not change anything, apart from increasing the number of available states. Some people may have thought that to be the full story in the time after K. von Klitzings discovery. But in May 1982, D. C. Tsui et al.[3] published a paper in which they reported the an extra plateau corresponding to a filling factor $\nu = 1/3$. Today we know that there are a lot of fractional states and not only in the first LL but also in the second LL ($2 < \nu < 4$). Fig. (1.6) shows a measurement of many fractional

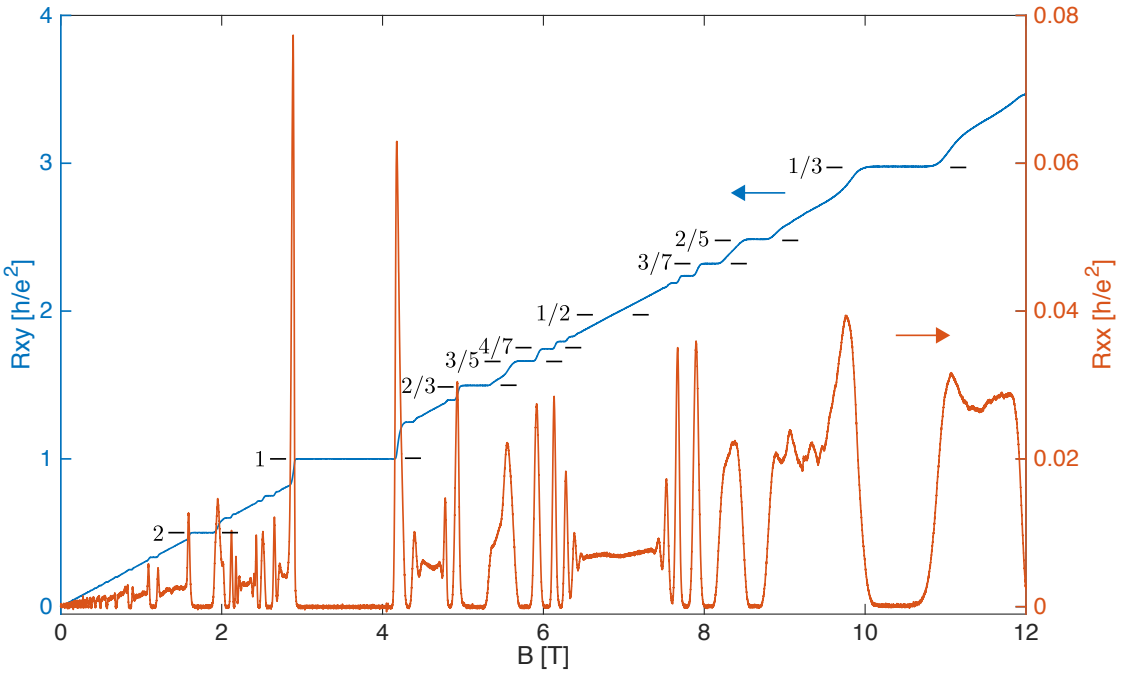

Figure 1.6: Measurement of the FQHE. Apart from all the integer plateaus, seen from 0-4T, a lot of fractional plateaus are also visible. $\nu = 1/2$, the symmetry point responsible for the development of the composite fermion theory is also labeled.

quantum Hall states.

Electron-electron interactions play a crucial role in the fractional quantum Hall effect. The interactions are needed in order to explain the emergence of a gapped ground state in a partially filled LL. Shortly after D. C. Tsui and colleagues discovery, R. B. Laughlin proposed a wavefunction that could explain the newly found fractional state[16]. It is widely believed that his wavefunction is the ground state wavefunction of all fractional states with a filling factor $\nu = 1/m$, m must be odd. The wavefunction, Laughlin proposed is:

$$\psi_{1/m} = \prod_{j<k} (z_j - z_k)^m \, e^{-\frac{1}{4}\sum_i |z_i|^2}, \tag{1.16}$$

where $z_k = x_k + iy_k$ is the complex coordinate of the electrons and $\prod_{j<k} (z_j - z_k)^m$ is called the Laughlin-Jastrow factor that insures a minimization of the Coulomb energy by vanishing if two electrons share the same coordinate. The exponent m has to be odd in order to insure a antisymmetric wavefunction under electron exchange.

A generally exciting outcome of Laughlins wavefunction is that excitations above this ground state carry a fractional charge, $e^* = e/m$.

There are many other fractional states that do not fall into the $1/m$ category. Several different schemes have been proposed in order to explain more than the $1/m$ states[17, 18, 19, 20], but the one that captures the most states are the Composite Fermion (CF) theory developed by J. K. Jain[4, 21]. The main motivation for the CF theory is found in the resemblance between the IQHE around small magnetic fields and the FQHE centered around $\nu = 1/2$, they are pretty much indistinguishable. It is strange that this resemblance even exists. The IQHE is to a very good approximation a single particle effect, whereas the FQHE is a very strongly correlated effect. The CF theory has the answer! It describes the FQHE as an IQHE for some new particles made from an electron and 2p flux quanta. Attaching 2 flux quanta to the electrons will completely remove the external magnetic field at $\nu = 1/2$, which means these new particles should behave like electrons in zero magnetic field. Amazingly, that is exactly what they do. This leads to the two most important equations within the CF theory:

$$\nu = \frac{\nu^*}{2p\nu^* \pm 1} \tag{1.17}$$

$$B^* = B - 2pn\phi_0. \tag{1.18}$$

Eq. (1.17) relates the CF filling factor, ν^*, to the electron filling factor, ν. The $\pm$ corresponds to positive/negative values of the effective magnetic field B^*, eq. (1.18). $\nu = 1/3$ is obtained by setting $2p = 2$ and $\nu^* = 1$ in eq. (1.17). This means that $\nu = 1/3$ for electrons is $\nu^* = 1$ for CF. There is a sequence that originate from $\nu = 1/2$, $\nu = 1/4$ and $\nu = 1/6$. The difference is how many flux quanta there is attached to each electron, 2, 4 or 6. Table (1.1) gives an overview of the main sequences. Whereas electrons order them selves in LL's, the newly created CF's order in Lambda Levels (ΛL). The ΛL's play the role of LL's for CF's.

ν/ν^*	1	2	3	4	5	6
ν	1/3	2/5	3/7	4/9	5/11	6/13
${}^{2p}\mathrm{CF}_{\nu^*}$	${}^2\mathrm{CF}_1$	${}^2\mathrm{CF}_2$	${}^2\mathrm{CF}_3$	${}^2\mathrm{CF}_4$	${}^2\mathrm{CF}_5$	${}^2\mathrm{CF}_6$
ν	1/5	2/9	3/13	4/17	5/21	6/25
${}^{2p}\mathrm{CF}_{\nu^*}$	${}^4\mathrm{CF}_1$	${}^4\mathrm{CF}_2$	${}^4\mathrm{CF}_3$	${}^4\mathrm{CF}_4$	${}^4\mathrm{CF}_5$	${}^4\mathrm{CF}_6$
ν	1/7	2/13	3/19			
${}^{2p}\mathrm{CF}_{\nu^*}$	${}^6\mathrm{CF}_1$	${}^6\mathrm{CF}_2$	${}^6\mathrm{CF}_3$			
ν	1	2/3	3/5	4/7	5/9	6/11
${}^{2p}\mathrm{CF}_{\nu^*}$	${}^2\mathrm{CF}_{-1}$	${}^2\mathrm{CF}_{-2}$	${}^2\mathrm{CF}_{-3}$	${}^2\mathrm{CF}_{-4}$	${}^2\mathrm{CF}_{-5}$	${}^2\mathrm{CF}_{-6}$
ν	1/3	2/7	3/11	4/15	5/19	6/23
${}^{2p}\mathrm{CF}_{\nu^*}$	${}^4\mathrm{CF}_{-1}$	${}^4\mathrm{CF}_{-2}$	${}^4\mathrm{CF}_{-3}$	${}^4\mathrm{CF}_{-4}$	${}^4\mathrm{CF}_{-5}$	${}^4\mathrm{CF}_{-6}$
ν	1/5	2/11	3/17			
${}^{2p}\mathrm{CF}_{\nu^*}$	${}^6\mathrm{CF}_{-1}$	${}^6\mathrm{CF}_{-2}$	${}^6\mathrm{CF}_{-3}$			

Table 1.1: Table connecting the ν to ν^*. Adapted from [4].

There exists fractions that can not be explained by any CF sequence, e.g. $\nu = 4/11$ and $\nu = 5/13$. These two fractions lie in between $\nu = 2/5$ and $\nu = 1/3$, so it would be convenient to describe them in terms of two flux quantum attachment, ^{2}CF states. The only way this is possible is by letting the ^{2}CF interact and form a FQH like ground state of ^{2}CF[4].

Another state that can not be described by a CF sequence is $\nu = 5/2$. In order to incorporate this into the CF theory we need to construct a BSC like parring of CF. This is done by G. Moore and N. Read[22], by introducing the wavefunction:

$$\psi_{5/2} = \mathrm{Pf}\left(\frac{1}{z_j - z_k}\right)\prod_{j<k}(z_j - z_k)^2\, e^{-\frac{1}{4}\sum_i |z_i|^2}, \tag{1.19}$$

where $\mathrm{Pf}(\frac{1}{z_j - z_k})$ is called the Pfaffian which is the antisymmetrized sum over all pairs $\frac{1}{z_j - z_k}$. Apart from the Pfaffian the wavefunction is the exact same as the Laughlin wavefunction, with one very important difference: The exponents are 2, not 3. The even exponents give the wavefunction the wrong exchange symmetry, but it is saved by the Pfaffian, which makes it fully antisymmetric.

Chapter 2

The Quantum Point Contact

2.1 Introduction

The quantum point contact (QPC) is one of the simplest structures that can be realized in a 2DEG by constraining it to a small region and thereby reducing the dimensionality of the system from 2D to 1D. Apart from being an interesting system in it self full of exciting physics, the QPC is also the fundamental "building block" of most other devices realized in 2DEGs. In quantum dots they are used as the "gate keepers" isolating the small island from the leads[23], they are used as charge detectors[24], and in electronic interferometers they play the role of the mirrors, partially reflecting incoming electrons[25].

A QPC can be defined by negatively charged strips of metal on the surface of a GaAs/AlGaAs heterostructure, so called top gates. The negatively charged gates deplete the electron gas underneath, thereby defining a 1D channel electrostatically see fig. (2.1).

In 1988, B. J. van Wees et. al[26] and D. A. Wharam et. al[27] both reported measurements of a QPC at cryogenic temperatures. They both found that the conductance through the QPC exhibited steps as a function of the applied gate

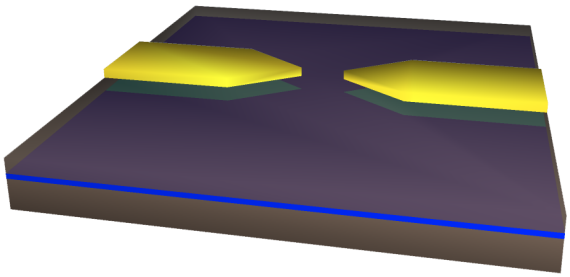

Figure 2.1: An illustration of a QPC defined on a GaAs/AlGaAs heterostructure. The 2DEG below is depleted when a negative voltage is applied to the gates.

voltage. They reported that the quantization of the conductance was described by

$$G = \frac{2e^2}{h}N, \tag{2.1}$$

where N is an integer depending on the gate voltage.

Even through the first QPCs where measured 26 years ago there are still aspects of the system that are not fully understood and subject to ongoing research. Of those the 0.7 anomaly is properly the most interesting. At elevated temperatures a plateau at $0.7 \times 2e^2/h$ develops, which can not be explained by a simple quantization in 1D. A lot of theory and data have been published in order to explain the anomaly including spontaneous spin polarization[28, 29], a Kondo-like correlated spin state[30, 31], and Wigner crystallization[32]. More resent measurements using scanning gate microscopy, does not provide more certainty as one measurement favors Kondo or Wigner physics[33], while another rule out localization effect as the origin of the 0.7 anomaly[34].

2.2 The conductance of a QPC

The quantization of the conductance through a QPC is only observed in the ballistic transport limit. The QPC is ballistic when the mean free path l_e of the electrons are much larger than the length L and width W of the QPC. Furthermore, the Fermi wavelength λ_F] must be comparable to the width of the QPC and the temperature

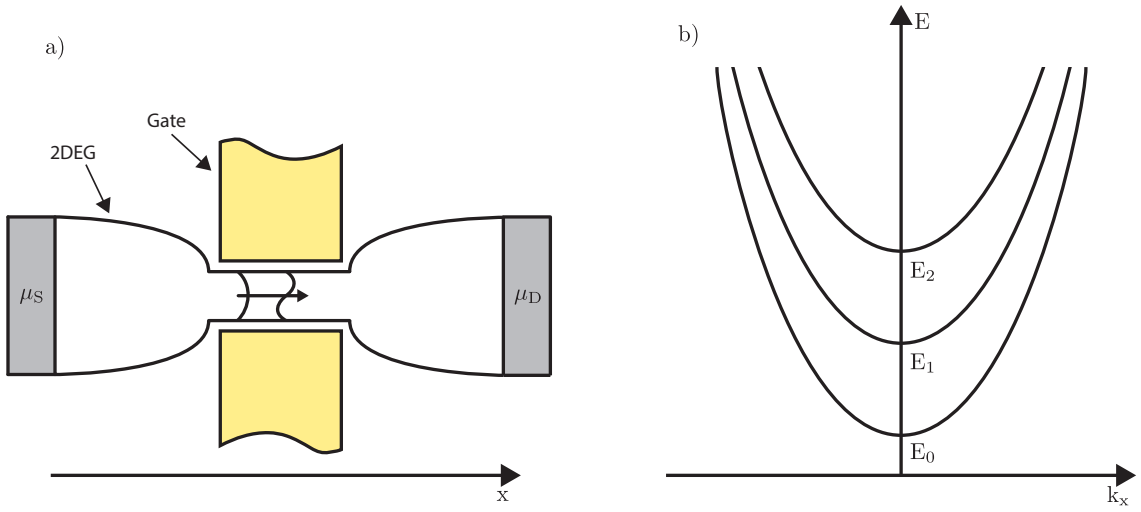

Figure 2.2: a) Schematic sketch of the QPC and contacts. b) A plot of subband energy versus wave vector k_x.

must be low compared to the level spacing ΔE of the transverse modes, defined by the confinement, in the QPC[12]. The full set of conditions are:

$$\begin{aligned} l_e &\gg L, W \\ \lambda_F &\approx W \\ \Delta E_n &\gg k_B T \end{aligned} \tag{2.2}$$

Assuming that the top gates produce a parabolic confinement potential and that the transition from QPC to 2DEG is smooth[35] (called the adiabatic approximation), we can write down a simple Hamiltonian to describe the system,

$$H = \frac{-\hbar^2}{2m^*}\left(\partial_x^2 + \partial_y^2\right) + eV(y). \tag{2.3}$$

Where $V(y)$ are the confinement potential in the y direction. The energies of the solution are:

$$E_n(x) = E_n + \frac{\hbar^2 k_x^2}{2m^*}, \tag{2.4}$$

where E_n is the energy of the n'th subband due to the confinement in the y-direction. Fig. (2.2) shows the dispersion along the x direction. The current density can be found by using the following formula:

$$j_{n,k_x}(x,y) = \frac{-|e|\hbar}{2im^*}\left[\psi^*_{n,k_x}(x,y)\nabla\psi_{n,k_x}(x,y) - \psi_{n,k_x}(x,y)\nabla\psi^*_{n,k_x}(x,y)\right]. \tag{2.5}$$

$\psi_{n,k_x}(x,y)$ is the wave function that solves eq. (2.3) and ∇ is the differential operator. The total current can then be found by integrating eq. (2.5) over k_x and summing over all subbands n.

In order to take the finite length of the QPC into account, a non-zero reflection coefficient must be incorporated. There is a finite scattering probability when an electron enters or exits the QPC. The reflection coefficient can be incorporated by looking at the current on the source side of the QPC, see fig. (2.2) for a sketch of the QPC and contacts. Right moving electrons ($k_x > 0$) originating from the source contact, occupied according to the Fermi-Dirac distribution of the source contact, all reach the QPC. Electrons moving left are either reflected electrons, described by the Fermi-Dirac distribution of the source contact, with probability $R_n(E)$ or transmitted electrons, from the drain contact described by the Fermi-Dirac distribution of the drain contact, with probability 1-$R_n(E)$. This all lead to[36]:

$$\begin{aligned} I &= 2|e|\sum_n \Big(\int_0^\infty \frac{dk_x}{2\pi} v_x(k_x) f(E-\mu_S) \\ &+ \int_{-\infty}^0 \frac{dk_x}{2\pi} v_x(k_x)\big[R_n(E) f(E-\mu_S) + (1-R_n(E))\, f(E-\mu_D)\big]\Big) \\ &= 2|e|\sum_n \int_0^\infty \frac{dk_x}{2\pi} v_x(k_x) T_n(E)\big[f(E-\mu_S) - f(E-\mu_D)\big], \end{aligned} \tag{2.6}$$

where $v_x(k_x) = \frac{\hbar k_x}{m^*}$ is the group velocity of the electrons, f is the Fermi-Dirac distribution of the source/drain contact, and the factor 2 comes from spin degeneracy. The transmission coefficient is related to the reflection coefficient by

$(1 - R_n(E)) = T_n(E)$. In general $T_n(E) = \sum_m |t_{mn}(E)|^2$ is the probability of transmitting through the QPC in mode n from all possible modes m at energy E. In the adiabatic approximation, where all modes are assumed to be decoupled, this simplifies to: $T_n(E) = |t_{nn}|^2$. Changing integration variable to energy $dk_x = \frac{dE}{\hbar v_x(k_x)}$ yields,

$$I = \frac{2|e|}{h} \int_{-\infty}^{\infty} dE \sum_n T_n(E) \big[f(E - \mu_S) - f(E - \mu_D) \big]. \tag{2.7}$$

It is clear from eq. (2.7) that the current will be zero without a bias applied, hence the Fermi-Dirac functions will cancel. Moving to Linear response and looking at small bias voltages, the Fermi-Dirac functions can be expanded: $f(E-\mu_S)-f(E-\mu_D) \approx -\frac{\partial f(E-\mu_S)}{\partial E}|e|V_{SD}$, where $|e|V_{SD} = \mu_S - \mu_D$. The final result for the conductance is:

$$G = \frac{I}{V_{SD}} = \frac{2e^2}{h} \int_{-\infty}^{\infty} dE \sum_n T_n(E) \left(-\frac{\partial f(E - \mu_S)}{\partial E} \right), \tag{2.8}$$

the last term reduced to a delta function in the limit $T \to 0$ and we get

$$G = \frac{2e^2}{h} \sum_n T_n(E). \tag{2.9}$$

If all transmission probabilities are 1 or 0, the sum reduced to N, the number of occupied modes, in agreement with eq. (2.1) observed in experiments. The width of the last factor in eq. (2.8) is $\approx 4k_BT$[37], so the steps disappear as the subband spacing ΔE approaches $4k_BT$.

2.3 Transport in lithographically square QPCs

In the following section I present transport measurements of square QPCs of different lengths. The QPCs are defined by Ti/Au top gates on a high mobility GaAs/AlGaAs quantum well heterostructure. The 2DEG has a bulk density of $n = 7.1 \times 10^{10}\,\mathrm{cm}^{-2}$

and a mobility of $\mu = 5.2 \times 10^6\,\mathrm{Vs/cm^2}$, measured in the dark.

The QPCs are designed to fulfill the two first constraints listed in eq. (2.2). The lengths of the QPCs measured are 600 nm and 800 nm respectively and the width of them both are 400 nm. The mean free path of the 2DEG electrons are $l_e \approx 23\,\mu\mathrm{m}$, which takes care of the first constraint. The Fermi wavelength is $\lambda_F \approx 100\,\mathrm{nm}$, which is close to the width of the QPCs. Fig. (2.3a) shows an SEM image of a QPC similar to the ones measured. Both QPCs measured has a middle gate, designed to change the local potential landscape. All measurement reported are with the middle gate fixed to ground.

All measurements were preformed in a cryofree dilution refrigerator with a base temperature of $\approx 10\,\mathrm{mK}$[1]. The conductance were measured using a 4-wire lock-in technique, with a small constant ac voltage bias of $V_{ac} < 10\,\mu\mathrm{V}$. Non-linear conductances were measured by applying a dc voltage up to $V_{dc} = \pm 2\,\mathrm{mV}$ on top of the small ac bias. The general measurement setup is shown in fig. (2.3b). The data

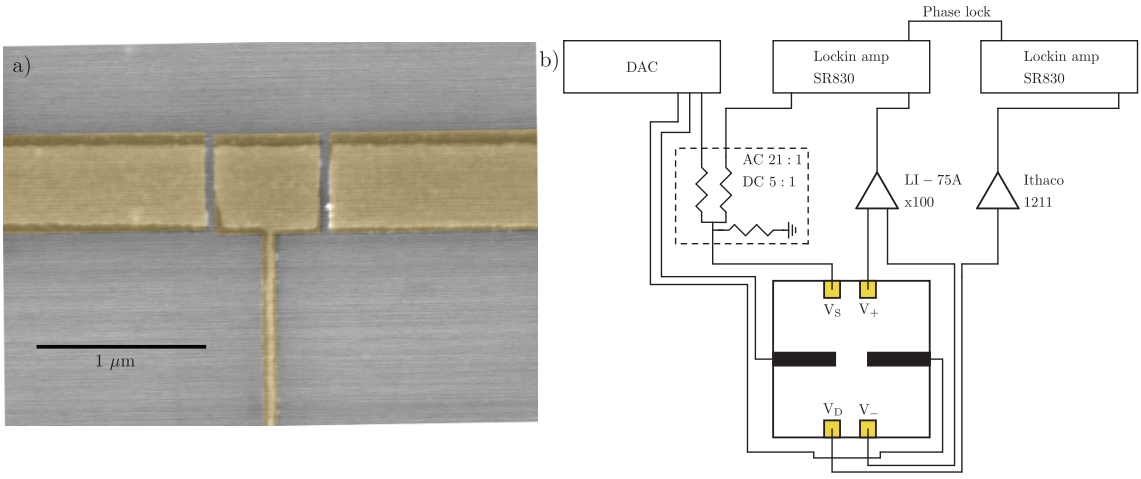

Figure 2.3: a) SEM image of a QPC similar to the two QPCs measured. b) Overview of the general measurement setup.

measured on both QPCs are quantitatively the same, therefore only data from the longer QPC are shown, unless otherwise stated.

Conductance quantization in both QPCs are shown in fig. (2.4a). The long

[1]Measured using a nuclear orientation thermometer.

QPC shows quantized steps until $\approx 15 \times 2e^2/h$, where as the short QPC only shows steps until $\approx 10 \times 2e^2/h$. Fig. (2.4b) shows the evolution of the conductance steps in the short QPC as the temperature is increased. At low temperature the conductance shows fully developed plateaus and a small hint of the 0.7 anomaly is visible. The 0.7 anomaly shows up as shoulder-like flattening of the conductance, just below the first spin degenerate plateau. At higher temperatures the regular steps become more washed out, because the energy of the thermal excitations is comparable to the level spacing. The 0.7 anomaly strengthen with temperature and it will persist to temperatures where all other plateaus are completely gone[38]. This "reversed" temperature dependence suggests that the 0.7 anomaly is not a ground state of the perfect transmitting system, but rather an emerging state in a not perfectly transmitting system, facilitated by some spin polarization mechanism[39], which still lacks a microscopic theoretical explanation.

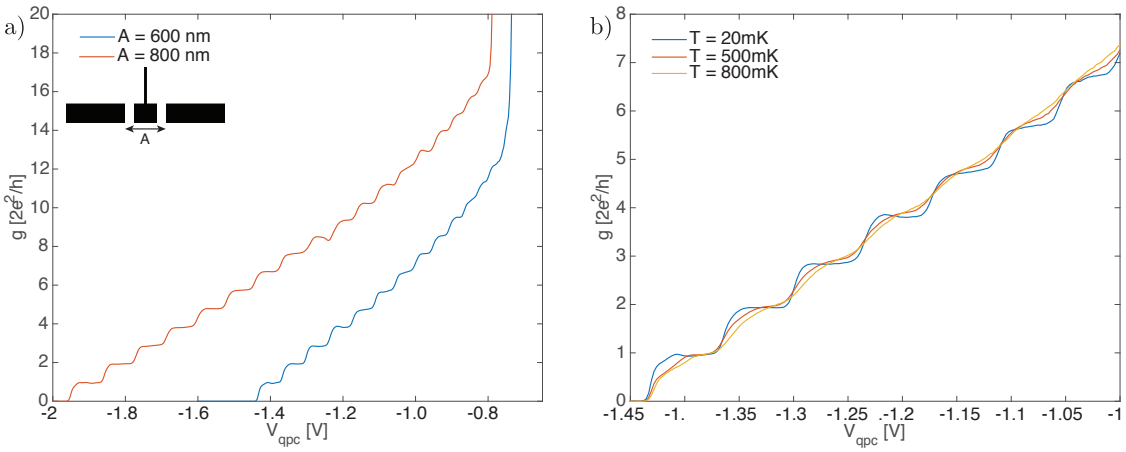

Figure 2.4: a) Conductance steps in the long (orange) and short (blue) QPC's. b) Temperature dependence of the conductance in the short QPC. The steps get less pronounced with higher temperature.

2.3.1 Non-linear transport

Non-linear transport data are shown in fig. (2.5a,b) as a waterfall plot, where each line is a conductance versus source/drain voltage trace. Each line is separated by $\Delta V_{qpc} \approx 1.8\,\mathrm{mV}$ and no artificial offset. Looking along $V_{sd} = 0\,\mathrm{mV}$ we find dense

clusters of lines whenever there is a plateau in the conductance. Moving to finite bias, $V_{sd} = \pm 1\,\mathrm{mV}$, we find "half" integer plateaus ($g = \{1/2, 3/2, 5/2\} \times 2e^2/h$) where there is an extra mode available on either the source or the drain side. The integer and half integer steps can be understood in the context of non-interacting electrons in a QPC, as schematically depicted in fig. (2.5c,d,e,f). When the source or drain chemical potential reach the first subband we see the first half conductance step plateau at finite bias, fig. (2.5c). Aligning the source and the drain to the hight of the first subband will bring us to the first conductance plateau at zero bias, fig. (2.5d). The $1.5 \times 2e^2/h$ plateaus are seen when the second subband is in between the two chemical potentials, fig. (2.5e). Finally raising both the source and the drain to the second subband pushes the conductance to $2 \times 2e^2/h$, fig. (2.5,f).

There are more line clusters in fig. (2.5a), the most prominent are the 0.7 anomaly, which at finite bias raises to $0.8 \times 2e^2/h$. At low temperatures the anomaly is not developed at $V_{sd} = 0\,\mathrm{mV}$, hence the clusters are only visible at finite bias. Connected to the lack of a plateau at $0.7 \times 2e^2/h$ is the zero bias anomaly (ZBA). The peaks between the first plateau and pinch-off (zero conductance though the QPC), seem to raise the conductance at zero bias, exactly making sure the plateau at $0.7 \times 2e^2/h$ does not form. At elevated temperatures the peaks die out and the 0.7 plateau start forming at zero bias, see fig. (2.5b). Zero bias peaks are also visible below the second plateau and if one looks closely a cluster-like formation of lines starts to develop at $g = 1.8 \times 2e^2/h$ on both sides of zero bias. The cluster-like formation persists at higher temperatures, fig. (2.5b). This is the second subband equivalent of the 0.7 structure.

The feature in the second subband is much weaker than the first subband counterpart, this could be due to screening by the fully transmitting first subband. Another interesting feature is the $1/2$ plateau, which persist to much higher bias than the higher half plateaus. It is also far from the expected conduction value, instead of $0.5 \times 2e^2/h$ it is found at $0.25 \times 2e^2/h$. There is one more striking difference between

the first half plateau and the rest: The higher plateaus all bend up with increasing bias, whereas the first is flat. S. Ihnatsenka et. al[40] can within their calculations explain both differences. The bending of the higher half plateaus is explained by screening effects of the lower fully transmitting subband modes. The local potential in the QPC show very little dependence on the bias voltage, which leads to an enhanced transmission of the partially reflected subband at finite bias. Furthermore, is the lower value of the half plateau found to originate from pinning effects. The lack of screening when only one subband is within the bias window, leads to an increase in electron-electron interaction, which in turn show pinning of the energy levels to the Fermi energy. Even taking these findings into account one can not explain the last feature in fig. (2.5a), the flat plateau at $g = 1.5 \times 2e^2/h$ and very high bias, $-2\,\mathrm{mV} < V_{sd} < -1.2\,\mathrm{mV}$. This plateau is only seen here and not at higher conduction values[2].

Another way of viewing the non-linear transport data is achieved by taking the derivative (numerically) of the conductance with respect to the gate voltage, $\partial g/\partial V_{qpc}$ called the transconductance. This highlights the transitions from plateau to plateau, seen as red strips. The plateaus are seen as big black (dark) diamond shaped areas. The first few integer and half integer plateaus are labeled in fig. (2.6a). Starting at the transition between the second and the third plateau, raising/lowering the chemical potential of the source corresponds to moving diagonally along the dotted blue line. Whereas the dotted green line marks the raising/lowering of the drain chemical potential. Following this method it is possible to map out almost all dark regions in fig. (2.6a). The remaining dark regions are the 0.7 structures, in the first and second subbands, marked by their finite bias conductance, $\approx 0.8 \times 2e^2/h$ and $\approx 1.8 \times 2e^2/h$. The extra 3/2 plateau is marked 1.5^*. The transitions lines between the 0.7 structure and the first plateau have a downward curvature, hinting to the different physical origin of this transition. A similar curvature is seen in

[2]This feature has also been observed by others[41, 42]

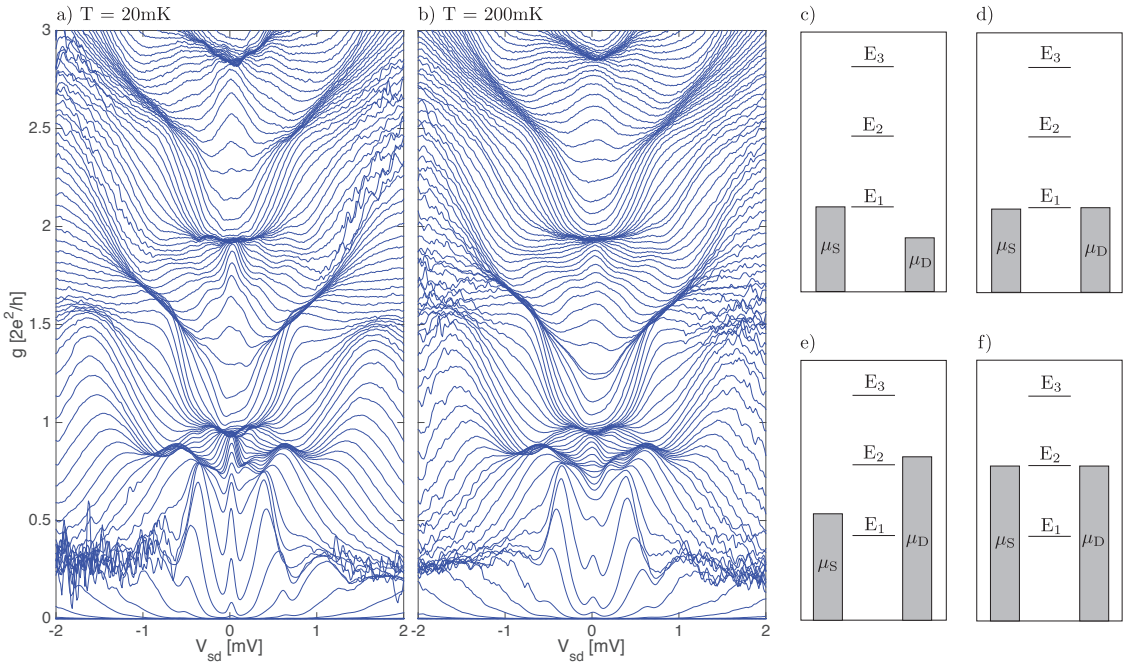

Figure 2.5: a) Waterfall plot of the non-linear differential conductance, at many different gate voltages. Dense clusters of lines indicate a plateau. The zero bias anomaly (ZBA) is clearly seen as peaks below $1 \times 2e^2/h$. The plateaus at $0.8 \times 2e^2/h$ and at $1.5 \times 2e^2/h$ at high bias are not expected when the non-interacting model. The 0.8 will at high temperature develop into the 0.7 structure. We speculate that the plateau at $1.5 \times 2e^2/h$ is closely connected to the 0.7 structure. b) Waterfall plot of the non-linear differential conductance at 200mK. The ZBA is almost gone and a small hint of the 0.7 plateau is visible at $V_{sd} = 0$. c)-f) Energy alignment with the source/drain chemical potentials span all the "normal" plateaus. c) Source/drain chemical potentials placed so the first plateau is visible. d)-e) Half plateaus are visible when a energy level lies in between the source/drain chemical potentials. f) When two energy levels lie below the source/drain chemical potentials, the second plateau is visible.

the transitions lines in the second subband. Fig. (2.6b,c) shows the regions with 0.7 structures in both QPCs. It is clear that the curved, 0.7 transition crosses the transition line between $1 \times 2e^2/h$ and $1.5 \times 2e^2/h$, seen as an enhancement of the transconductance. Furthermore, it cuts the $1.5 \times 2e^2/h$ diamond in two, leaving two $1.5 \times 2e^2/h$ plateaus. One of the curved transition lines are marked by a thin green guiding line, fig. (2.6c). The enhancement of the transconductance is also visible in the second subband, but the transition is too weak in order for a second $2.5 \times 2e^2/h$ plateau to form. The two $1.5 \times 2e^2/h$ plateaus are vastly different. The "normal" plateau is bending, whereas the new is flat. This means that the screening by the

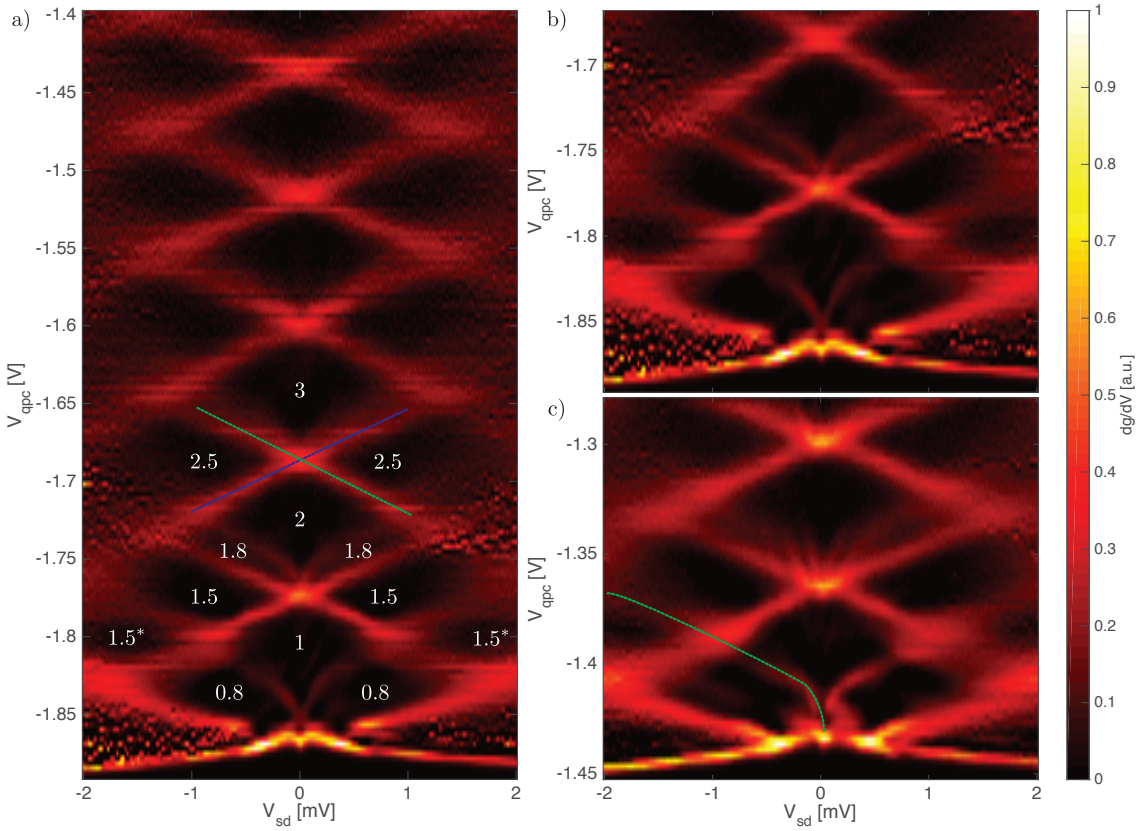

Figure 2.6: a) Transconductance ($\partial g/\partial V_{qpc}$) as a function of V_{sd}, in the long QPC. Dark regions mark plateaus and red lines the transition between them. The first few plateaus are marked by there conductance. The 0.8 and 1.8 regions are connected the to emergence of a 0.7 structure (in both subbands) at higher temperatures. The extra 1.5 plateau (marked 1.5*) seems to be related to the 0.7 structure in the first subband. b) Zoom in of data from the long QPC. A clear enhancement of the transconductance is visible when the 0.7/1 transition crosses the 1/1.5 transition, cuting the 1.5 plateau into two. c) Zoom in of the same region, in data from the short QPC. The same features are also seen in this QPC. The left transition line is marked by a green guide line.

lower subband is balanced by some extra mechanism, which makes the local QPC potential drop linearly with bias, as needed for a flat plateau.

Information about the subband spacing can be extracted from the widths of the zero bias plateau diamonds. Within linear response ($V_{sd} \approx 0$) the following equation holds for the difference in chemical potentials: $\mu_s - \mu_d = V_{sd}|e|$. This leads to an equation for the subband spacing: $\Delta V_{sd} = 2\Delta E_{sb}/|e|$, where ΔV_{sd} is the width of the diamond along V_{sd}, see fig. (2.6a). Because the diamonds have the same size through the whole range, from $g = 0 \times 2e^2/h$ to $g = 7 \times 2e^2/h$, the individual level

spacings are also the same. Equidistant level spacing is exactly the fingerprint of a harmonic confinement potential. The level spacing of the long QPC is 1.1 meV, whereas the short QPC have a level spacing of 1.45 meV.

2.4 Conclusion

I have measured two different QPC's, one with a length of 800 nm the other a bit shorter, only 600 nm long. We find nice conductance plateaus until $15 \times 2e^2/h$ in the long QPC and $10 \times 2e^2/h$ in the short. Non-linear transport revealed the existence of a 0.7 structures in the two lowest subbands, as well as an extra $1.5 \times 2e^2/h$ plateau at high bias. We argue that the formation of this extra plateau must involve extra mechanisms to balance the screening by the lower subband and is closely connected to the 0.7 structure in the first subband. Finally we find that the confiment potential in both QPCs are highly harmonic, resulting in an equidistant level spacing of 1.1 meV and 1.45 meV for the long and short QPC respectively.

Chapter 3

Quasi Particle Tunneling

3.1 Introduction

One of the most amazing things about the FQHE is the fractionally charged quasi particles found in all fractional states. These quasi particles are gap less excitations above the ground state that emerges when the system is moved away from a quantized plateau. Moving to the low field side of a plateau will decrease the degeneracy of the LL and leave an excess of electrons, which in the CF picture can be seen as an quasi particle. A quasi hole will be generated on the high field side of a plateau where there is an excess of magnetic field quanta[4]. We will from now on not distinguish between quasi particle and hole, but simply call them quasi particles. Fig. (3.1) show the transition from $\nu = 1/3$ to $\nu = 2/5$ in terms of CF's.

From Laughlin's wave function we get that the charge of the quasi particles in 1/m, m odd, fractions should be $e^* = e/m$[16]. Jain has with the CF theory extended this argument to all fractions produced in the CF sequences. In general a fraction $\nu = \nu^*/(2p\nu^* \pm 1)$ will have quasi particles with charge $e^* = e/(2p\nu^* \pm 1)$[4]. This result implies that all 3rd fractions (1/3, 2/3, 4/3, 5/3) have a quasi particle charge of $e^* = e/3$. Experimentally this has not always been the case. The quasi particle charge at $\nu = 2/3$ have been measured to be $e^* = 2e/3$ using an antidot and

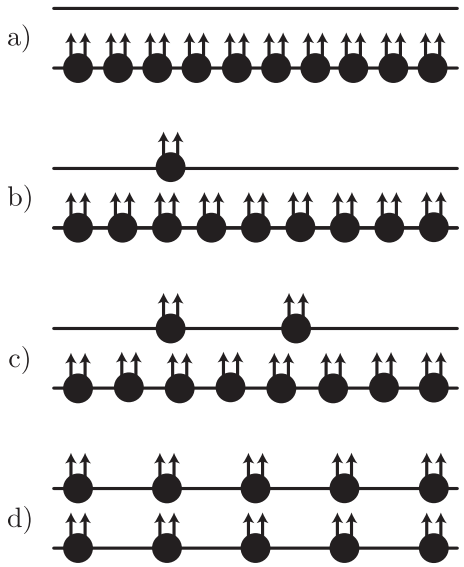

Figure 3.1: Transition from $\nu = 1/3$ to $\nu = 2/5$. a) The system is in the $\nu = 1/3$ state, all CF are in the first ΛL. b) As the field deviates from the exact filling the degeneracy of the ΛL's decrease and a single CF is pushed to the second ΛL. c) This process continues when the field is further reduced. d) The $\nu = 2/5$ state is reached when the two lowest ΛL's are filled.

in shot noise measurements[43, 44]. Others have measured the quasi particle charge to be $e^* = e/3$[45] and it therefore suggests that more work is needed in order to fully understand if the general theory is correct.

In this chapter we present measurements of quasi particle tunneling in a QPC. We present data in both the weak backscattering (WB) and the strong backscattering (SB) regime. In the WB regime quasi particles are tunneling between edge channels in the QPC. The QPC allow us to bring the two edge channels into close proximity and thereby obtaining a non zero tunneling coupling. The transmission coefficient of the tunneling edge channels should only be reduced by a few percent in order to remain in the WB regime. In the SB regime will the tunneling be across the QPC, where the transmission coefficient is almost zero. The tunneling particles in this regime are electrons, because they have to tunnel through a vacuum region in the QPC. Both situations are schematically depicted in fig. (3.2).

The theory describing the physics controlling tunneling in the WB regime was developed by X. G. Wen[46, 25]. The tunneling conductance as a function of the

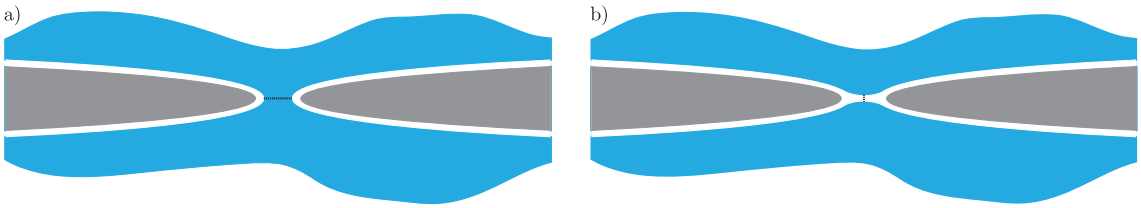

Figure 3.2: Schematically sketch of the two different tunneling regimes. Blue regions are a QH fluid and the white regions are depleted 2DEG, achieved by applying a negative voltage to the two gates (gray). a) The weak backscattering regime. Here the edge states of the QH fluid is weak backscattered across the constriction, marked by the black dashed line. b) The strong backscattering. The 2DEG in the constriction is completely depleted and tunneling happens along the QPC.

source/drain voltage is given by:

$$g_{tun}(V_{sd},T) = AT^{2g-2}F\left(g,\frac{e^*V_{sd}}{k_BT}\right) \tag{3.1}$$
$$F(g,x) = B\left(g+i\frac{x}{2\pi},g-i\frac{x}{2\pi}\right)\times \left(\pi\cosh\left(\frac{x}{2}\right)-2\sinh\left(\frac{x}{2}\right)\mathrm{Im}\left\{\Psi\left(g+i\frac{x}{2\pi}\right)\right\}\right),$$

where A is a constant, B is the beta function, Ψ is the digamma function, e^* is the fractional quasi particle charge and g is the Coulomb interaction parameter. Tacking the hight of the tunneling peak at different temperatures allow us to extract the Coulomb interaction parameter, g, without fitting the full functional form of eq. (3.1). This is possible because eq. (3.1) at $V_{sd}=0$ gives $g_{tun}(0,T)\propto T^{2g-2}$. e^* can only be found by fitting to the full functional form of eq. (3.1). In practice we never measure the conductance but the resistance. The two can be related by[47]

$$g_{tun} = \frac{R_D - R_{xy}}{R_{xy}^2}, \tag{3.2}$$

where R_D is the a measure of the local filling factor in the QPC given by $R_D = \frac{1}{\nu_c}\frac{h}{e^2}$[37]. If the bulk and constriction are not at the same filling factor, R_{xy} can in eq. (3.2) be exchanged with R_∞, the resistance at high source/drain voltage. At high source/drain voltage can the tunneling contribution to the resistance be neglected,

which mean that $R_D(V_{sd} \neq 0) \rightarrow R_{xy}$ or R_∞ if the bulk and constriction are not aligned.

For the SB case the theory was developed by several people[48, 49]. Later A. V. Shytov et al.[50] expanded the theory to include tunneling into a compressible quantum Hall edge, filling in the gaps left by the first theories that only dealt with incompressible edges. The theory predicts that the tunneling current, I_{tun}, for a voltage bias between the two edges shall follow a power law dependence

$$I_{tun} \approx V^\alpha, \tag{3.3}$$

at low temperature, $eV \gg k_B T$. Furthermore, shall the linear conductance exhibit a nonlinear dependence on temperature

$$G(T) \approx T^{\alpha-1}. \tag{3.4}$$

The exponent α is predicted to show a stepwise increases as a function of $1/\nu$ (ρ_{xy}), see fig. (3.3). For $0 < 1/\nu < 1$ the predicted exponent is 1 (full curve not shown

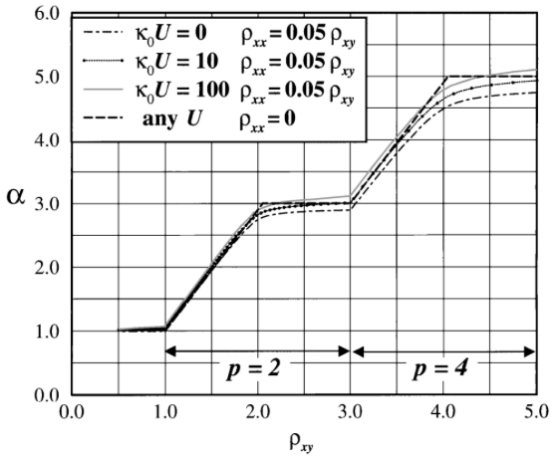

Figure 3.3: Power law exponent, α, as a function of $1/\nu$ (ρ_{xy}). α shows a stepwise dependence on the inverse of the filling factor. Steps appear when the relative magnetic field felt by the CF shifts negative to positive. If ρ_{xx} is not zero, the shape of the curve depends on the strengths of the short range interactions, U. Taken from [50].

in the figure), for $1 < 1/\nu < 2$ α increases linearly to 3 where it plateaus until $1/\nu = 3$. The onset of the plateau is due the sign change of the effective magnetic field felt by the CF's. The value p indicated on the figure is equal to the 2p factor in eq. (1.17), which count the number of flux quanta attached to each electron. Four different curves are shown, three curves show the deviation away from the simple result without any longitudinal resistivity. Here U and κ_0 is a short range interaction and the CF compressibility.

3.2 The weak backscattering regime

A lot of data have been published on measurements of the quasi particle charge associated with a large range of different fractions. The first tunneling data published were mostly focused on $\nu = 1/3$, which according to theory should have a quasi particle charge $e^* = e/3$ and a Coulomb interaction parameter $g = 1/3$[51, 52]. These early papers did not report any extracted numbers for the quasi particle charge, but did find $g = 1/3$. The quasi particle charge of $e^* = 1/3$ was measured in Shot-noise measurements some years before the first tunneling measurements were reported[53, 54].

Apart from $\nu = 1/3$, a single reported measurement of $\nu = 1/5$ has been published[55], whereas much attention have been given $\nu = 5/2$, because of the possibility that this fraction will carry quasi particles with non-Abelian exchange statistics[56, 57, 58, 59, 47, 60].

We will focus on tunneling measurements of the quasi particle charge associated with $\nu = 1/3$. In the following section we present tunneling measurements of two square QPCs of different lengths, 800 nm and 600 nm respectively. The QPCs are defined by Ti/Au top gates on a high mobility GaAs/AlGaAs quantum well heterostructure. The 2DEG has a bulk density of $7.1 \times 10^{10}\,\mathrm{cm}^{-2}$ and a mobility of $5.2 \times 10^{6}\,\mathrm{cm}^2/\mathrm{Vs}$, measured in the dark.

All measurements were preformed at cryogenic temperatures, using a cryofree di-

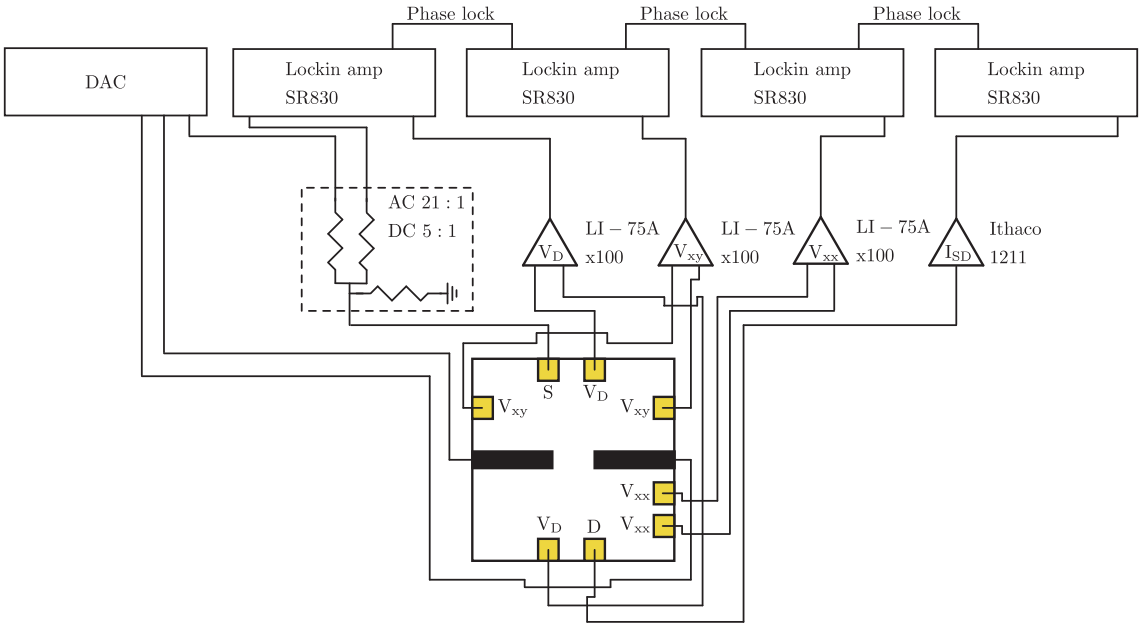

Figure 3.4: The measurement setup consists of four lock-in amplifiers, all phase locked, measuring the the three voltages R_{xx}, R_{xy} and R_D. The last lock-in are used to measure the current through the sample. All voltage signals goes through a pre-amplifier with a very low noise floor before entering the lock-in's. The current is converted to a voltage signal through a current amplifier. The voltage on the QPC gates are delivered by a DAC, which also feeds the dc voltage used in nonlinear measurements.

lution refrigerator with a base temperature, $T \approx 10\,\mathrm{mK}$. The resistances, both bulk and the local QPC resistance, R_D, were measured using a 4-wire lock-in technique, with a small ac bias, $V_{ac} < 10\,\mu\mathrm{V}$ applied. Nonlinear tunneling data were measured using an additional dc bias, $V_{dc} = \pm 1\,\mathrm{mV}$ along with the ac bias. The measurement setup is shown in fig. (3.4). The setup allows for simultaneous measurements of R_{xy}, R_{xx} and R_D. An SEM image of a similar QPC as the ones measured can be seen in fig. (2.3a).

Fig. (3.5a) shows the bulk resistances, R_{xy} and R_{xx} in the full magnet range (0 T-12 T). We see many well developed fractions, as well as $\nu = 1/3$ at 12T. Fig. (3.5b) show a zoom in of R_{xy} around $\nu = 1/2$, along with the resistance of the QPC, R_D, with $-0.8\,\mathrm{V}$ on the short QPC gates. The bulk and constriction densities does not match when the QPC gates are depleted. We see hints of tunneling in R_D

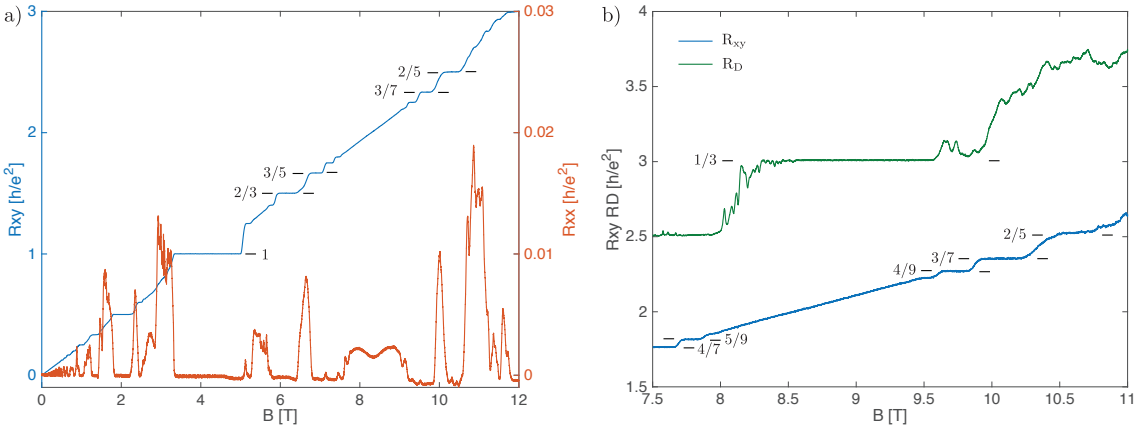

Figure 3.5: a) Bulk measurement of R_{xy} and R_{xx} as a function of magnetic field, B. $\nu = 1/3$ can just be reached in the bulk at 12 T. b) Zoom-in at region around $\nu = 1/2$ in the bulk. R_D shows the filling of the QPC which is energized at -0.8 V.

at the end of $\nu_c = 1/3$, where the plateau develops two small consecutive bumps. These tunneling features strongly suggest that we are able to measure tunneling of $\nu = 1/3$ quasi particles even though they only live in the close vicinity of the QPC. Similar behavior is seen in the longer QPC as well.

Looking at the nonlinear behavior of these tunneling peaks provide the needed

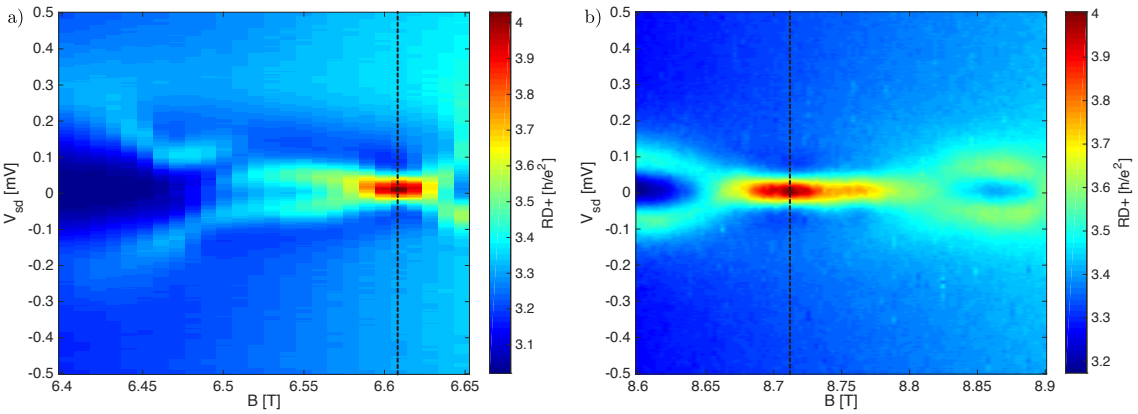

Figure 3.6: a) 2D surface plot of a tunneling peak in the short QPC. Dark region to the left is the end of $\nu_c = 1/3$ The slight darkening of on the sides of the tunneling peak indicates an undershoot. b) Similar plot for the long QPC.

information to determine the origin of the features seen at zero bias. We are looking for zero bias peaks that emerge right when the plateau stops, which is exactly the place where quasi particles are created and where the fully transmitting edge states start to turn around, i.e. finite backscattering. Two 2D surface plot of R_D as a

function of V_{sd} and B on the high side of $\nu_c = 1/3$ are shown in fig. (3.6). Fig. (3.6a) shows data from the short QPC, where the gates are held at $-1.21\,\mathrm{V}$. The data shown in fig. (3.6b) is from the long QPC, with the gates held at $-1.28\,\mathrm{V}$. In both cases a tunneling peak raises to $\approx 4e^2/h$ right after the plateau ends. The peaks stretches over $\approx 100\,\mathrm{mT}$ which is also the length others have observed (for other fractions)[57, 59]. It is also wroth noticing that both peaks have a small undershoot on both sides, seen as a slightly darker blue region. These undershoots are characteristic for tunneling peaks in the WB regime and are seen for fractions with a Coulomb interaction parameter, g, below 1/2.

The non-peak feature seen in fig. (3.6b), at $\approx 8.87\,\mathrm{T}$ is also present in the data from the short QPC (not seen in fig. (3.6a)) and there are in general a lot of smaller alternating dips and peaks further away from the $\nu = 1/3$ plateau in both devices. These features suggests that other mechanisms also are at play. The fact that the tunneling peaks are seen just after the plateau ends and that they stretch over a long range in field, makes us more confident that these other mechanisms does not alter the tunneling significantly.

Fig. (3.7) shows the result of fitting the tunneling peaks, from fig. (3.6), to eq. (3.1). Fig. (3.7a,b) shows the 1D cuts, taken along the dashed lines in fig. (3.6a,b), at several temperatures. Inserts show the peak hight as a function of temperature. The peak hight is defined as the distance from peak max to the peak base line, R_∞. The hight follow a power law dependence, $\propto T^{2g-2}$, where g is the Coulomb interaction parameter. For the two tunneling peaks we find g to be 0.43 and 0.51 for the short and long QPC respectively. The result of fitting the data in fig. (3.7b) are shown in fig. (3.7c), here six different temperatures are shown. The fits are obtained by simultaneously fitting all the curves in fig. (3.7b) and minimizing, in the least square sense, with respect to A, g, R_∞ and e^*/e. We are only interested in g and e^*/e, which are the physical parameters we can relate to theoretical predictions. The best fit parameters are $(g, e^*/e) = (0.61, 0.31)$. The

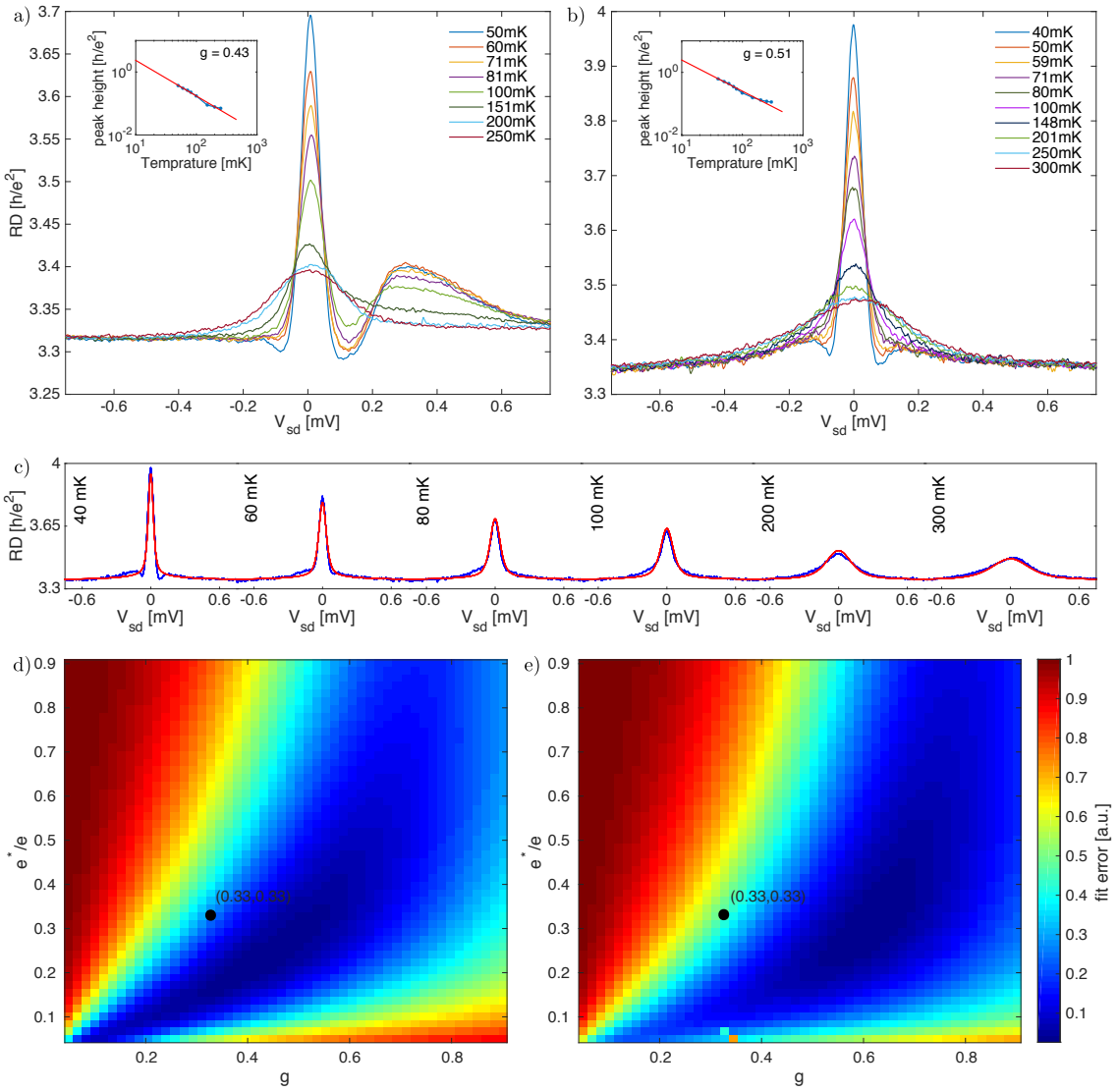

Figure 3.7: a)+b) Tunneling peak as a function of source drain voltage, for multiple temperatures. Data are taken at the positions of the dashed lines in fig. (3.6). Inserts show the peak heights as a function of temperature. The height follow a power law, giving values for g. For the short QPC (fig. (3.7a)) we obtain g = 0.43 and g = 0.51 is extracted for the long QPC. c) Result of fitting eq. (3.1) to the data in fig. (3.7b). Best fit parameters are $(g, e^*/e) = (0.51, 0.31)$. d)+e) Fit error as a function of g and e^*/e. Error is obtained as the sum of the squared residuals, normalized by the maximum error.

data in fig. (3.7a) are fitted in the same way (not shown), with one exception. The extra bump developing at smaller temperatures around $V_{sd} = 0.3\,\mathrm{mV}$ are not included in the fit. The bump is always seen in the this QPC, although we have no good explanation to why or what courses it. The best fit parameters obtained for the data in fig. (3.7a) is $(g, e^*/e) = (0.43, 0.23)$.

Fig. (3.7d,e) show normalized fit errors as a function of g and e^*/e. The plots are obtained by fixing g and e^*/e and then fitting for the best A and R_∞. The sum of the squared residuals, normalized to the maximum error value, are used to indicate the best fit. The theoretical predicted values for g and e^*/e, $(g, e^*/e) = (1/3, 1/3)$, are marked on both figures.

We find reasonable agreement between the g extracted from the peak height and the g given directly from the fit to eq. (3.1). The values for e^* obtained are both close to the predicted value, $e^* = 1/3$. The predicted value for $g = 1/3$, is not in accordance with our values for g. The values obtain for g, from the two data samples, are also not close to the same value. We speculate that this spread in g may have to do with the non-peak features mentioned earlier. If the quasi particles tunnel through a more complicated landscape, and not just from edge to edge, it may alter the effective interaction but it should not alter the charge of the tunneling particles itself.

3.3 The strong backscattering regime

When X. G. Wen[61] predicted that the edge state excitations in the fractional quantum Hall regime could be described as a chiral Luttinger liquid[62], he started avalanche of experimental and theoretical research. One of the first experimental papers to be published on the subject was by F. P. Milliken et al.[63]. They looked at tunneling through a QPC while holding the bulk at $\nu = 1/3$. They found at lot of sharp resonances that decayed and narrowed rapidly with temperature. Especially was it found that the FWHM of the resonances decreased with a power law described by the exponent 2/3. This result was on of the first that showed the X. G. Wens prediction was true. Shortly after A. M. Chang et al.[64] reported I-V measurements supporting the results found by F. P. Milliken. They utilized a new type of sample grown by L. N. Pfeiffer, the cleaved edge overgrowth technique (CEOG).

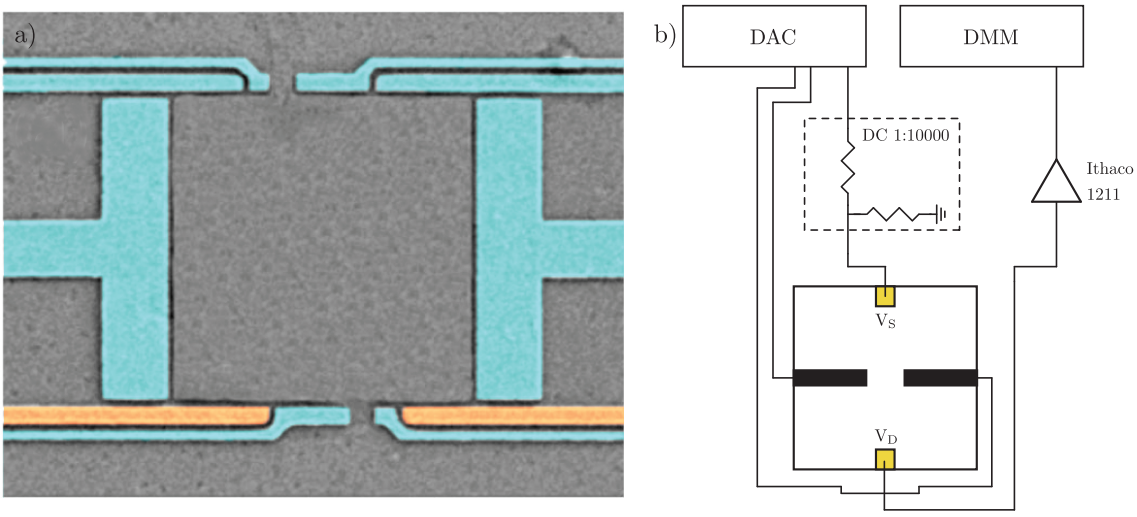

Figure 3.8: a) SEM image of a similar the device as the one measured. b) Only the two gates highlighted in orange were used, the rest were fixed to ground. b) The measurement setup used to measure tunneling in the SB regime.

This type of sample have a much cleaner tunneling barrier, than one can produce with a QPC. The CEOG type of samples have become a standard system for these type of measurements. A. M. Changs found the voltage exponent in eq. (3.3) for $\nu = 1/3$, to be 2.7 and the temperature exponent in eq. (3.4) to be 1.75, consistent with theory.

To everybodys surprise was it by 1997 clearly established that experiment and theory only agreed in the case of $\nu = 1/3$ and $\nu = 1$, which was shown to have a exponent $\alpha = 1$ (not a Luttinger liquid). M. Grayson et al.[65] reported measurements on 4 samples that together with some new data from Chang showed a linear increase in α starting from $\nu = 1$ and not a stepwise increase as predicted, see fig. (3.3). Recently M. Hike et al.[66] have measured the transition from Fermi liquid to Luttinger liquid in the vicinity of $\nu = 1$. They showed that $\alpha = 1$ all the way from $B \approx 0$ to $\nu = 1$, confirming that part of the theory.

We present measurements in the SB regime probed with a QPC defined on a high mobility GaAs/AlGaAs quantum well heterostructure, with a density of $8.9 \times 10^{10}\,\mathrm{cm}^{-2}$ and a mobility of $25 \times 10^{6}\,\mathrm{cm}^{2}/\mathrm{Vs}$. The sample is cooled in a cryofree dilution refrigerator, with a base temperature of $\approx 10\,\mathrm{mK}$. The tunneling

measurements are done by applying a dc voltage $V_{sd} = \pm 1mV$ and measuring the current in a dmm, through a current amplifier. No ac bias was applied to the sample during the measurements. Fig. (3.8a) shows the setup used. The dc bias and QPC gates were controlled by a DAC (digital/analog converter) with a max output of $\pm 10V$. A similar device as the one used are shown in fig. (3.8b). Only the two gates highlighted in orange were used, while all other gates were fixed to ground.

The QPC were operated in the range of -2V to -3V in order to achieve a tunneling barrier across the QPC. The QPC pinches off at $\approx -3.7\,\mathrm{V}$ and in the voltage range used 4-8 spin degenerate modes were seen in zero field measurements of the QPC.

The results are highlighted in fig. (3.9). a) shows an I-V measurement of the tunneling curve with $\nu = 1/3$ in the bulk. The black line is the best fit to the slope, which gives an exponent $\alpha = 3.75 \pm 0.15$. A similar measurement with $\nu = 1$ in the bulk are shown in the insert. The extracted value for α is 1.03 ± 0.001. The value for α found for $\nu = 1$ agree with a already know fact, the QH fluid at the integers are Fermi liquids and should therefore have linear I-V curves. Theory predicts that the exponent for $\nu = 1/3$ should be 3. The measured value is some what consistent with the theory value. Others have reported tunneling exponents that are not consistent from sample to sample[66, 67] which indicate that these tunneling exponents are very sensitive to the barrier shape.

Fig. (3.9b) shows a set of I-V curves at different temperatures taken at an intermediate filling fraction $\nu = 0.26$. At the highest temperatures the I-V curves are almost linear. Fitting the linear regime of the tunneling curves (flat parts around zero bias) allows an extraction of the linear conductance G. The value found for G are plotted in fig. (3.9c), where a power law fit gives the best exponent. Theory tells us that we can relate the voltage exponent found by fitting single I-V curves with the exponent extracted from the linear conductance. The linear conductance exponent are according to eq. (3.4) given by $\alpha - 1$. Using this relation gives $\alpha = 2.13 \pm 0.18$.

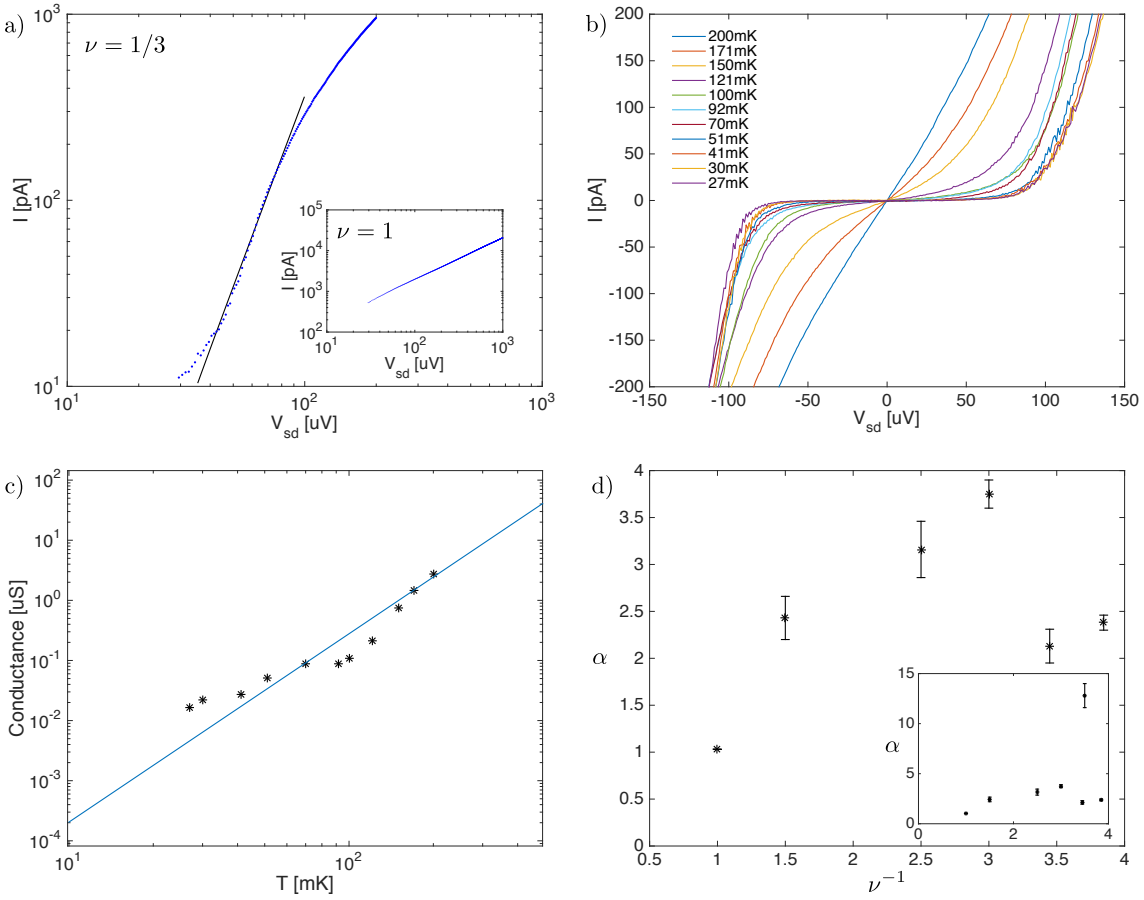

Figure 3.9: a) I-V curve for $\nu = 1/3$ in the bulk. The extracted value for α is 3.75 ± 0.18. The insert show the same measurement for $\nu = 1$, here α is 1.03 ± 0.001. b) I-V curves for a large range of temperatures. c) Values of the linear conductance obtained from fit the the I-V curves in b). The exponent found can theoretically be related to the voltage exponent. d) Values for α plotted as a function of inverse filling. The values found at $\nu = 1, 2/3, 2/5, 1/3$ all fall on a straight line. Insert also show that value obtained for $\nu = 2/7$.

Fig. (3.9d) shows all the values for α found both on well defined fractions and off. The insert also shows the value for α obtained at $\nu = 2/7$. Ignoring the $\nu = 2/7$ value for a second, the four value found at $\nu = 1, 2/3, 2/5, 1/3$ all fall on the straight line as seen by others[64, 66, 65]. These four values are all from single I-V curves, whereas the last two values at low filling both are obtained via the linear conductance. We therefore find that the theoretically found relation between the two exponents not are supported by our data. As for $\nu = 2/7$, we speculate that we have hit a resonance, which would alter the tunneling signal profoundly.

3.4 Conclusion

I have measured quasi particle tunneling in the $\nu = 1/3$ state in two QPCs of different length. Both gave fractional charges close to the predicted value, $e^* = 0.31e$ and $e^* = 0.23e$. The Coulomb interaction parameter g was not found to be consistent with theory, but reasonable agreement was found between g values extracted from peak height fit and the full fit. I speculate that the effective interaction may be altered by multiple tunneling event or by other interactions as the quasi particles tunnel.

Several fractions are measured in the strong backscattering regime. I found that values of α found from single I-V curves fall on a straight line and that this data does not support the theoretical link between the voltage exponent and the exponent found from the linear conductance.

Appendix A

Device Fabrication

When first encountering the world of semiconductor based sample fabrication, you will properly find yourself completely overwhelmed. Not only because there are so many new things to learn, also peoples apparent attention to detail will likely seem unnecessary or even crazy to begin with. You will soon learn that the attention to detail is the single most important part of fabrication. It is the details that guide you when trying out new designs or when a fabrication step fails, which they will. Writing everything down is therefore crucial, also when things go as according to plan.

This section contains the recipes I have used, along with my comments and consideration. Most of the recipes are in many ways very similar to the ones found in Douglas McClures Ph.D thesis[68]. As these served as a starting point for my fabrication.

A.1 Removal of Ga from the backside of the wafer

All GaAs wafers are grown on a blank GaAs substrate. A blank GaAs substrate is the best starting point, because it insures a perfect crystal without defects or strain from the first atomic layer. In order to glue the substrate to the holder inside the

MBE (Molecular beam epitaxy), pure Ga are used.
Because Ga has a very low melting point, 29.8 °C, the backside of the wafer will constantly change and might cause problems during fabrication. Removing the Ga is therefore the first step in any fabrication process.

1. Spin a single layer of your favorite photo resist on the top side of the wafer. I use AZ4511, spun at 4000 rpm for 45 s.
2. Bake at 115 °C for 2 min.
3. Place the wafer face down on a clean room wipe and wipe off as much Ga you can (should be almost al of it). It can be necessary to reheat the Ga, but do it on a colder hot plate, so you do not hard bake the resist.
4. Etch in HCl (full strength) for ~3 min. Etch time depend on the amount of Ga left on the backside.
5. Rinse in MQ to stop the etch.
6. Rinse off the resist in Acetone. Hold the wafer over a beaker and use a squeeze bottle to remove most of the resist. This prevents any Ga from sticking on the top surface.
7. Strip resist fully by soaking in Acetone for 10 min.

It is very important to be careful that no Ga ends up on the surface of the wafer. It is impossible to remove, without damaging the surface and may completely ruin the part of the wafer it landed on. Before starting this fabrication procedure, you must have received the correct acid training.

A.2 Mesa formation

The first step is to cleave a suitable size chip off of the wafer. A good size is 6 mm by 7 mm. This leaves room for 16 mesas of standard size with enough space to the

sides, that the outer most mesas are sufficiently far away from the cleaved edges. There are two ways to cleave a piece off a wafer. Using a scriber insures high precession, but may leave a lot of small particles along the scribe, which can be very hard to get off again. If precession is not a problem, I strongly recommend cleaving by making a small "notch" at the very edge. If one applies a bit of force, while resting the notch over a sharp edge, the chip will break along a crystal direction, leaving a nice clean cut.

Mesas are so big that e-beam lithography is overkill and will take a very long time. With photo lithography the time spend on this step is reduced from many hours, to 1 hour.

I will recommend using a piece of pure GaAs as a test chip throughout the hole mesa formation process, in order to test the etch rate before etching the real chip. The junk chip can also come in handy because it stops you from wasting a chip in case of bad resist or old developer.

1. Three solvent clean. Sonicate for 4 min in TCE (trichloroethylene), acetone and IPA (isopropanol). Below dry with nitrogen.

2. Bake at 185 °C for 5 min, in order to thoroughly dry the chip.

3. Spin a single layer of AZ4511 at 4000 rpm for 45 s.

4. Bake at 115 °C for 2 min.

5. Expose the chip in the mask aligner for 10 s (100 µJ/cm^2).

6. Develop in 1:3 AZ400K/H_2O for 60 s. Contentiously move the chip around in the developer.

7. Rinse in water for 15 s and blow dry with nitrogen.

8. Etch in 240:8:1 H_2O:H_2O_2:H_2SO_4. Etch the junk chip for 60 s.

9. Rinse in H_2O for 15 s. Blow dry with nitrogen.

10. Strip the resist on the junk chip, by soaking it in acetone for 10 min. Rinse in IPA and blow dry with nitrogen.

11. Measure the mesa hight using the Profilometer, the etch rate should be roughly 3 nm/s.

12. Etch the real chip, using the precise rate.

13. Strip the resist on real chip, by soaking it in acetone for 10 min. Rinse in IPA and blow dry with nitrogen.

14. Measure the mesa hight on the real chip.

The hight of the mesas are needed when connecting top gates and bond pads.
It is important to let the etch rest for at least 15 min before using it. I recommend using a magnet stirrer. For most wafers it is sufficient to etch past the first donor layer, in order to isolate the mesas at cryogenic temperatures. If the second donor layer (below the 2DEG) is heavily doped, it may be necessary to etch all the way past that donor layer as well. Just as with the Ga removal procedure, it is important that you have received the correct acid training before starting this fabrication step.

A.3 Ohmic contacts

Next step after formation of the mesas are ohmic contacts. The contacts have to be annealed and that process may damage any small gates, which is why the ohmic contact patterning must come first.
The contacts are so large, 135 µm×135 µm, that photo lithography is well within range. Nevertheless we have all ways used e-beam lithography, because it is a extremely reliable process.

1. Three solvent clean. Sonicate for 4 min in TCE (trichloroethylene), acetone and IPA (isopropanol). Below dry with nitrogen.

2. Bake at 185 °C for 5 min, in order to thoroughly dry the chip.
3. Spin a layer of PMMA 495 A8, at 4000 rpm for 45 s.
4. Bake at 185 °C for 4 min.
5. Spin a layer of PMMA 495 A8, at 4000 rpm for 45 s.
6. Bake at 185 °C for 6 min.
7. Spin a layer of PMMA 950 A4, at 4000 rpm for 45 s.
8. Bake at 185 °C for 8 min.
9. Pattern using the Elionix ELS-F100, acceleration voltage 100 kV, beam current 40 nA, 250 µm aperture, 600 µm write field, 20 k dots, dose 1200 µ C/cm^2.
10. Develop in 1:3 MIBK/IPA for 90 s.
11. Rinse in IPA for 15 s and blow dry with nitrogen.
12. Plasma clean for 60 s.
13. Prepare the metal evaporator for loading. The next steps must be done fast.
14. Etch in 7% HF for 5 s, in order to remove any oxide.
15. Rinse in H_2O for 10 s and blow dry with nitrogen.
16. Run to the evaporator, load the sample and pump out the load lock. You can take it easy from now on.
17. Evaporate the appropriate amount of metal. See A.3.1.
18. Lift off in 80 °C NMP (n-methyl-2-pyrrolidone) for 60 min.
19. Using a small pipette, gently blow warm NMP over the chip (still in the beaker) to remove most or all the unwanted metal. If some does not come of, transfer the chip to room temperature acetone for a few hours.

20. Finish lift off by rinsing in IPA. Blow dry with nitrogen.

21. Anneal sample in the AccuThermo AW610 rapid thermal annealer. See A.3.2.

The tri-layer resist stack is very high, ~1200 nm, which is needed for the metal stack forming the ohmic contacts. For most metal stacks, it is properly sufficient to use a single layer of A8 under the A4, but I have found that it reduces likelihood of getting a nice and easy lift off.
HF is a serious chemical, which needs special attention. You should always have somebody with you in the clean room, when using HF. The extra person have the added advantage, that he/she can load the chip into the evaporator immediately after the etch, while you clean up.

A.3.1 Metal stacks for ohmic contacts

We have had success with two different metal stacks, Pt-Ge-Au and Ni-Ge-Au. Although lately the Pt based metal stack have been given us some problems. The chip gets very hot when evaporating Pt and it causes the A8 resist to reflow, which shifts the position of the window in the different resist layers. Because the Ni based stack also gives us good contact, we have abandoned the Pt based stack.
The most important aspect in a Ge-Au based contact stack is the ratio between Ge and Au, it should always be 1:2. This ratio forms an eutectic alloy that have been proven to be vital when forming ohmic contact to GaAs(*ref to Williams*). The Pt/Ni serves as a wetting agent and is believed to enhance the diffusion of Ge into the GaAs, which makes the contact to the 2DEG. A top layer of Au makes the Pt/Ni move efficient, but it also provides a contact surface that is easy to bond to.

Ni-Ge-Au Because of the Ni this metal stack has to be evaporated using the old E-gun evaporator.

1. 5 nm Ni

2. 135 nm Ge
3. 270 nm Au
4. 112 nm Ni
5. 100 nm Au

This stack gives a good contact (~200 Ω) to 2DEG's located, down to, 250 nm below the surface. If the 2DEG is located below 250 nm, we have had success with increasing the thickness of the top layer to 150 nm.

Pt-Ge-Au This metal stack can be evaporated using either AJA's (ATC 1800-HY). Be aware that the chip heats up when evaporating Pt, keep the rate low.

1. 5 nm Pt
2. 200 nm Au
3. 100 nm Ge
4. 73 nm Pt
5. 100 nm Au
6. 50 nm Ge
7. 55 nm Pt

Because this metal stack was only used a few times, it is an exact reblica of the recipe used by Douglas McClure[68].

A.3.2 Anneal recipes

The anneal recipe we use is adapted from a recipe developed by James Medford[69]. We always anneal in a Forming gas (N_2/H_2) atmosphere and we use nitrogen as flushing gas. The final temperature and time depends on the wafer. We have used

temperatures between 400 °C and 460 °C and annealing times between 20 s and 2 min. A good starting point, which is almost always close to a good time/temperature pair, is 60 s at 440 °C.

The recipe as it is defined in the RTP (AccuThermo AW610) can be found below. The actual annealing step is #11.

#	Function	Time (s)	Temperature (°C)	N_2 (slpm)[1]	N_2/H_2 (slpm)
1	Delay	30	0	5.0	0.0
2	Delay	30	0	0.0	2.0
3	Ramp	20	120	0.0	2.0
4	Steady	50	120	0.0	2.0
5	Ramp	20	220	0.0	2.0
6	Steady	20	220	0.0	2.0
7	Ramp	10	300	0.0	2.0
8	Ramp	10	360	0.0	2.0
9	Steady	20	360	0.0	2.0
10	Ramp	20	440	0.0	2.0
11	Steady	60	440	0.0	2.0
12	Delay	120	0	0.0	3.0
13	Delay	700	0	5.0	0.0

Table A.1: Anneal recipe

A.4 ALD - Oxides

It can be a good idea to put down a layer of oxide, using the ALD, before any top gates, especially if you need positive gate voltages. The easiest is just to put a layer covering the hole chip, because this saves a e-beam step and it is easy to bond through the oxide layer.

We have found that gate bond pads does not stick to the chip surface and will come off very easily, when bonding, if there is oxide between the bond pad and chip. I therefore recommend putting down resist and opening windows where the oxide is needed. ALD oxide covers all surfaces, so even though the actual layer is only a few nm thick, it can be hard to lift off. Using more then one layer of resist usually helps.

[1] standard litres per minute

There are generally one parameter that matters when growing oxides, the temperature. Increasing the temperature will allow the process to go faster, but will also incorporate more stacking faults/imperfections. I have always grown my oxides at 90 °C, but higher temperatures may also give working oxides.

HfO_2 This recipe gives good oxides on both ALD machines.

1. Inner and Outer heaters set to 90 °C. Let them stabilize.
2. Set N_2 flow to 20 sccm.
3. Pulse Hf precurser for 0.2 s.
4. Wait 60 s.
5. Pulse H_2O for 0.02 s.
6. Wait 60 s.
7. Repeat 3. to 6. until desired hight is reached.
8. Turn off heaters and N_2 flow.

The hight of one layer is ~1.2 Å.

A.5 Top gates

Putting down top gates is last step before the chip is done and ready to cool down. I have always done this step in two rounds. First defining the small gate on top of the mesa and in a second step connecting to bond pads. The bond pads are big and need much more metal, than the small gates, in order insure reliable bonding. It may seem like the wrong order at first, but the small gates can easily break if you try putting them on top of the much thicker bond pad arm.

A.5.1 Small gates

In order to save time on the e-beam step, I only expose the smallest features with a low current. I use 100 pA or 500 pA depending on the size and how close the features are to each other. You should only use 100 pA if your features, or separation between features, are 50 nm or less. For bigger features ($\geq$1 µm) I use 2 nA.
For the low current, use 40 µm aperture, 150 µm write field, 60 k dots, dose 2400 µC/cm^2.
For the high current use, 60 µm aperture, 300 µm write field, 60 k dots, dose 1800 µC/cm^2.
The doses are roughly correct if the PMMA are developed in 0 °C MIBK/IPA. Cold development gives sharper definition, which is crucial if the design involves small separations.

1. Three solvent clean. Sonicate for 4 min in TCE (trichloroethylene), acetone and IPA (isopropanol). Below dry with nitrogen.
2. Bake at 185 °C for 5 min, in order to thoroughly dry the chip.
3. Spin a layer of PMMA 950 A2, at 4000 rpm for 45 s.
4. Bake at 185 °C for 15 min.
5. Pattern using the Elionix ELS-F100, acceleration voltage 100 kV.
6. Develop in 0 °C MIBK/IPA 1:3 for 90 s.
7. Rinse in room temperature IPA for SI15s and blow dry with nitrogen.
8. Evaporate 5 nm Ti and 15 nm Au.
9. Lift off in Acetone over night.
10. If necessary use nitrogen bobbles to remove all the metal. DO NOT Sonicate.

A.5.2 Bond pads

It is in general easiest to evaporate enough metal on the bond pads and arms so the total metal stack is taller than the mesa, this insures contact to the small gates on top of the mesa. If the mesa is very tall, this approach will quickly involve evaporating a lot of gold, which is expensive. Instead I have sputtered a layer of titanium, which insures that the metal climbs the mesa wall nicely, see figure A.1.

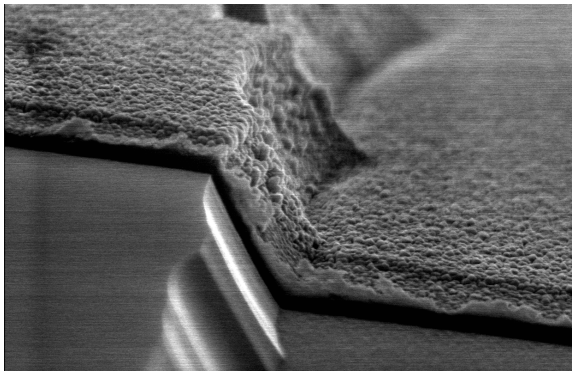

Figure A.1: A picture of a tall mesa with Ti/Au climbing the side wall. 100 nm of Ti is first sputtered at an 30° angle, followed by evaporation of 200 nm of Au.

1. Three solvent clean. Soak for 4 min in TCE (trichloroethylene), acetone and IPA (isopropanol). Below dry with nitrogen. NO sonication.

2. Bake at 185 °C for 5 min, in order to thoroughly dry the chip.

3. Spin a layer of PMMA 495 A8, at 4000 rpm for 45 s.

4. Bake at 185 °C for 4 min.

5. Spin a layer of PMMA 495 A8, at 4000 rpm for 45 s.

6. Bake at 185 °C for 6 min.

7. Spin a layer of PMMA 950 A4, at 4000 rpm for 45 s.

8. Bake at 185 °C for 8 min.

9. Pattern using the Elionix ELS-F100, acceleration voltage 100 kV, beam current 40 nA, 250 µm aperture, 600 µm write field, 20 k dots, dose 1200 µ C/cm^2.

10. Develop in 1:3 MIBK/IPA for 90 s.

11. Rinse in IPA for 15 s and blow dry with nitrogen.

12. Plasma clean for 60 s.

13a. **Use for short mesas.** Evaporate 100 nm Ti and enough Au so it the metal stack is 5%-10% taller than the mesa.

13b. **Use for tall mesas.** Sputter 100 nm Ti at a 30° angle and rotating at 40 rpm, followed by evaporating 200 nm Au.

14. Lift off in 80 °C NMP (n-methyl-2-pyrrolidone) for 60 min.

15. Using a small pipette, gently blow warm NMP over the chip (still in the beaker) to remove most or all the unwanted metal. If some does not come of, transfer the chip to room temperature acetone for a few hours.

16. Finish lift off by rinsing in IPA. Blow dry with nitrogen.

Bibliography

[1] Bardeen, J., Cooper, L. N. & Schrieffer, J. R. Microscopic theory of superconductivity. *Physical Review* **106**, 162 (1957).

[2] Mott, N. F. The basis of the electron theory of metals, with special reference to the transition metals. *Proceedings of the Physical Society A* **62**, 416 (1949).

[3] Tsui, D. C., Stormer, H. L. & Gossard, A. C. Two-dimensional magnetotransport in the extreme quantum limit. *Physical Review Letters* **48**, 1559 (1982).

[4] Jain, J. K. *Composite Fermions* (Cambridge University Press, 2007).

[5] Goerbig, M. O., Lederen, P. & Smidth, C. M. Competition between qauntum-liquid and electron-solid phases in intermediate landua levels. *Physical Review B* **69**, 115327 (2004).

[6] Davies, J. H. *The Physics of Low-Dimensional Semiconductors* (Cambridge University Press, 2006).

[7] Manfra, M. J. Molecular beam epitaxy of ultra-high quality algaas/gaas heterostructures: Enabling physics in low-dimensional electronic systems. *arxiv:1309.2717* (2013).

[8] Grinberg, A. A. & Shur, M. S. Effect of image charges on impurity scattering of two-dimensional electron gas in algaas/gaas. *Journal of Applied Physics* **58**, 382 (1985).

[9] Shur, M. *GaAs Devices and Circuits* (Plenum Press, 1987).

[10] Hall, E. On a new action of the magnet on electric currents. *American Journal of Mathematics* **2**, 287 (1879).

[11] Drude, P. Zur elektronentheorie der metalle. *Annalen der Physik* **306**, 566 (1900).

[12] Ihn, T. *Semiconductor Nanostructures* (Oxford University Press, 2010).

[13] von Klitzing, K., Dorda, G. & Pepper, M. New method for high-accuracy determination of the fine-structure constant based on quantized hall resistance. *Physical Review Letters* **45**, 494 (1980).

[14] Halperin, B. I. Quantized hall conductance, current-carrying edge states, and the excitence of extended states a in two-dimensional disordered potential. *Physical Review B* **25**, 2185 (1982).

[15] Chklovskii, C. D., Shklovskii, B. I. & Glazman, L. I. Electrostatics of edge channels. *Physical Review B* **46**, 4026 (1992).

[16] Laughlin, R. B. Anomalous quantum hall effect: An incompressible quantum fluid with fractionally charged excitations. *Physical Review Letters* **50**, 1395 (1983).

[17] Haldane, F. D. M. Fractional quantization of the hall effect: A hierarchy of incompressible quantum fluid states. *Physical Review Letters* **51**, 605 (1983).

[18] Halperin, B. I. Statistics of qausiparticles and the hierarchy of fractional quantized hall states. *Physical Review Letters* **52**, 1583 (1984).

[19] Zhang, S. C., Hansson, T. H. & Kivelson, S. Effective-field-thoery model for the fractional quantum hall effect. *Physical Review Letters* **62**, 82 (1989).

[20] Girvin, S. M. & MacDonald, A. H. Off-diagonal long-range order, oblique confinement, and the fractional quantum hall effect. *Physical Review Letters* **58**, 1252 (1987).

[21] Jain, J. K. Composite-ferimon approach for the fractional quantum hall effect. *Physical Review Letters* **63**, 199 (1989).

[22] Moore, G. & Read, N. Nonabelions in the fractional quantum hall effect. *Nuclear Physics B* **360**, 362 (1991).

[23] Lindemann, S., Ihn, T., Heinzel, T., Zwerger, W. & Ensslin, K. Stability of spin states in quantum dots. *Physical Review B* **66**, 195314 (2002).

[24] Petta, J. R., Johnson, A. C., Taylor, J. M., Laird, E. A., Yacoby, A., Lukin, M. D., Marcus, C. M., Hanson, M. P. & Gossard, A. C. Cohernt manipulation of coupled electron spins in semiconductor quantum dots. *Science* **309**, 2180 (2005).

[25] de C. Chamon, C., Freed, D. E., Kivelson, S. A., Sondhi, S. L. & Wen, X. G. Two point-contact interferometer for quantum hall systems. *Physical Review B* **44**, 2331 (1997).

[26] van Wees, B. J., van Houten, H., Beenakker, C. W. J., ans L. P. Kouwenhoven, J. G. W., van der Marel, D. & Foxon, C. T. Quantized coonductance of point contacts in two-dimensional electron gas. *Physical Review Letters* **60**, 848 (1988).

[27] Wharam, D. A., Thornton, T. J., Newbury, R., Pepper, M., Ahmed, H., Frost, J. E. F., Hasko, D. G., Peacock, D. C., Ritchie, D. A. & Jones, G. A. C. One-dimensional transport and the quantisation of the ballistic resistance. *Journal of Physics C: Solid State Physics* **21**, L209 (1988).

[28] DiCarlo, L., Zhang, Y., McClure, D. T., Reilly, D. J., Marcus, C. M., Pfeiffer, L. N. & West, K. W. Shot-noise signature of 0.7 structure and spin in a quantum point contact. *Physical Review Letters* **97**, 036810 (2006).

[29] Thmoas, K. J., Nicholls, J. T., Simmons, M. Y., Pepper, M., Mace, D. R. & Ritchie, D. A. Possible spin polarization in a one-dimensional electron gas. *Physical Review Letters* **77**, 135 (1996).

[30] Iqbal, M. J., Levy, R., Koop, E. J., Dekker, J. B., de Jong, J. P., van der Velde, J. H. M., Reuter, D., Wieck, A. D., Aguado, R., Meir, Y. & van der Wal, C. H. Odd and even kondo effects from emergent localization in qauntum point contacts. *Nature* **501**, 79 (2013).

[31] Cronenwett, S. M., Lynch, H. J., Goldhaber-Gordon, D., Kouwenhoven, L. P., Marcus, C. M., Hirose, K., Wingreen, N. S. & Umansky, V. Low-temperature fate of the 0.7 structure in point contact: A kondo-like correlated state in an open system. *Physcial Reveiew Letters* **88**, 226805 (2002).

[32] Matveev, K. A. Conductance of a quantum wire at low electron density. *Physical Review B* **70**, 245319 (2004).

[33] Brun, B., Martins, F., Faniel, S., Hackens, B., Bachelier, G., Cavanna, A., Ulysse, C., Ouerghi, A., Gennser, U., Mailly, D., Huant, S., Bayot, V., Sanquer, M. & Sellier, H. Wigner and kondo physics in quantum point constacts revealed by scanning gate microscopy. *Nature Communications* **5**, 4290 (2014).

[34] Iagallo, A., Paradiso, N., Roddaro, S., Reichl, C., Wegscheider, W., Biasiol, G., Sorba, L., Beltram, F. & Heun, S. Scanning gate imaging of quantum point contacts and the origin of the 0.7 anomaly. *Nano Research* **8**, 948 (2015).

[35] Glazman, L. I., Lesovik, G. B., Khmel'nitskii, D. E. & Shekter, R. I. Reflectionless quantum transport and fundamental ballistic-resistance steps in microscopic constrictions. *JETP Letter* **48**, 238 (1988).

[36] Nazarov, Y. V. & Blanter, Y. M. *Quantum Transport: Introduction to Nanoscience* (Cambridge University Press, 2009).

[37] Beenakker, C. W. J. & van Houten, H. Quantum transport in semiconductor nanostructures. *Solid State Physics* **44**, 1 (1991).

[38] Cronenwett, S. M. *Coherence, Charging, and Spin Effects in Quantum Dots and Point Contacts*. Ph.D. thesis, Stanford University (2001).

[39] Bruus, H., Cheianov, V. V. & Flensberg, K. The anomalous 0.5 and 0.7 structure plateaus in quantum point contacts. *Physica E* **10**, 97 (2001).

[40] Ihnatsenka, S. & Zozoulenko, I. V. Origin of the '0.25 anomaly' in the nonlinear conductance of a qauntum point contact. *Physical Review B* **79**, 235313 (2009).

[41] Kristensen, A., Bruus, H., Hansen, A. E., Jensen, J. B., Lindelof, P. E., Marckmann, C. J., Nygård, J. & Sørensen, C. B. Bias and temperature dependence of the 0.7 conductance anomaly in quantum point contacts. *Physical Review B* **62**, 10950 (2000).

[42] DiCarlo, L., Zhang, Y., McClure, D. T., Reilly, D. J., Marcus, C. M., Pfeiffer, L. N. & West, K. W. Shot-noise signatures of 0.7 structure and spin in a quantum point contact. *Physical Review Letters* **97**, 026810 (2006).

[43] Kou, A., Marcus, C., Pfeiffer, L. N. & West, K. W. Coulomb osillacations in antidots in the integer and fractional quantum hall regimes. *Physical Review Letters* **108**, 256803 (2012).

[44] Bid, A., Ofek, N., Heiblum, M., Umansky, V. & Mahalu, D. Shot noise and charge at the 2/3 composite fractional quantum hall state. *Physical Review Letters* **103**, 236802 (2009).

[45] Martin, J., Ilani, S., Verdene, B., Smet, J., Umansky, V., Mahalu, D., Schuh, D., Abstreiter, G. & Yacoby, A. Localization of fractionally charged quasiparticles. *Science* **305**, 980 (2004).

[46] Wen, X. G. Edge transport properties of the fractional quantum hall states and weak-impurity scattering of a one-dimensional charge-density wave. *Physical Review B* **44**, 5708 (1991).

[47] Lin, X., Dillard, C., Kastner, M. A., Pfeiffer, L. N. & West, K. W. Mesurements of qausiparticle tunneling in the $\nu = \frac{5}{2}$ fractional quantum hall state. *Physical Review B* **85**, 165321 (2012).

[48] Wen, X. G. Theory of the edge states in fractional quantum hall effect. *International Journal of Modern Physics B* **6**, 1711 (1992).

[49] Kane, C. L. & Fisher, M. P. A. Impurity scattering and transport of fractional quantum hall edge states. *Physical Review B* **51**, 13449 (1995).

[50] Shytov, A. V., Levitov, L. S. & Halperin, B. I. Tunneling into the edge of a compressible quantum hall state. *Physical Review Letters* **80**, 141 (1998).

[51] Roddaro, S., Pellegrini, V., Beltram, F., Pfeiffer, L. N. & West, K. W. Particle-hole symmetric luttinger liquids in a quantum hall circuit. *Physical Review Letters* **95**, 156804 (2005).

[52] Roddaro, S., Pellegrini, V., Beltram, F., Biasiol, G., Sorba, L., Raimondi, R. & Vignale, G. Nonlinear quasiparticle tunneling between fractional quantum hall edges. *Physical Review Letters* **90**, 046805 (2003).

[53] de Picciotto, R., Reznikov, M., Heiblum, M., Umansky, V., Bunin, G. & Mahalu, D. Direct observation of a fractional charge. *Nature* **389**, 162 (1997).

[54] Saminadayar, L., Glattli, D. C., Jin, Y. & Etienne, B. Observation of the e/3 fractionally charged laughlin quasiparticle. *Physical Review Letters* **79**, 2526 (1997).

[55] Roddaro, S., Pellegrini, V. & Beltram, F. Interedge strong-to-weak scattering evolution at a contriction in the fractional quantum hall regime. *Physical Review Letters* **93**, 046801 (2004).

[56] Miller, J. B., Radu, I. P., Zumbühl, D. M., Levenson-Falk, E. M., Kastner, M. A., Marcus, C. M., Pfeiffer, L. N. & West, K. W. Fractional quantum hall effect in a quantum point contact at filling fraction 5/2. *Nature Physics* **3**, 561 (2007).

[57] Radu, I. P., Miller, J. B., ans M. A. Kastner, C. M. M., Pfeiffer, L. N. & West, K. W. Quasi-particle porperties from tunneling in the $\nu = 5/2$ frational quantum hall state. *Science* **320**, 899 (2008).

[58] Willett, R. L., Pfeiffer, L. N. & West, K. W. Alternation and interchange of e/4 and e/2 period interference oscillations consistent with filling factor 5/2 non-abelian quasiparticles. *Physical Review B* **82**, 205301 (2010).

[59] Bear, S., Rössler, C., Ihn, T., Reichl, C. & Wegscheider, W. Experimental probe of topological orders and edge excitations in the second landau level. *Physical Review B* **90**, 075403 (2014).

[60] Dolev, M., Heiblum, M., Umansky, V., Stern, A. & Mahalu, D. Observation of a quarter of an electron charge at the $\nu = 5/2$ quantum hall state. *Nature* **452**, 829 (2008).

[61] Wen, X. G. Chiral luttinger liquid and the edge excitations in the fractional quantum hall states. *Physical Review B* **41**, 12838 (1990).

[62] Haldane, F. D. M. 'luttinger liquid theory; of one-dimensional quantum fluids: I. properties of the luttering model and their extension to the general 1d interacting spinless fermi gas. *Journal of Physics C: Solid State* **14**, 2585 (1981).

[63] Milliken, F. P., Umbach, C. P. & Webb, R. A. Indications of a luttinger liquid in the fractional quantum hall regime. *Solid State Communications* **97**, 309 (1996).

[64] Chang, A. M., Pfeiffer, L. N. & West, K. W. Obervation of chiral luttinger behavior in electron tunneling into fractional quantum hall edges. *Physical Review Letters* **77**, 2538 (1996).

[65] Grayson, M., Tsui, D. C., Pfeiffer, L. N., West, K. W. & Chang, A. M. Continuum of chiral luttinger liquids at the fractional quantum hall edge. *Physical Review Letters* **80**, 1062 (1997).

[66] Hike, M., Tsui, D. C., Pfeiffer, L. N. & West, K. W. Experiments on the fermi to tomonaga-luttinger liquid transition in quasi-1d systems. *Journal of the Physical Society of Japan* **72 (Sup A)**, 92 (2003).

[67] Turley, P. J., Druist, D. P., Gwinn, E. G., Maranowski, K., Campmann, K. & Gossard, A. C. Tunneling through point contacts in the quantum hall effect. *Physica B* **249-251**, 410 (1998).

[68] III, D. T. M. *Interferometer-Based Studies of Quantum Hall Phenomena*. Ph.D. thesis, Harvard University (2012).

[69] Medford, J. R. *Spin Qubits in Double and Triple Quantum Dots*. Ph.D. thesis, Harvard University (2013).